

1 **COVID-19 virtual patient cohort reveals immune mechanisms driving disease outcomes**

2 Adrienne L. Jenner<sup>1,2</sup>, Rosemary A. Aogo<sup>3</sup>, Sofia Alfonso<sup>4</sup>, Vivienne Crowe<sup>5</sup>, Amanda P. Smith<sup>3</sup>,  
3 Penelope A. Morel<sup>6</sup>, Courtney L. Davis<sup>7</sup>¶, Amber M. Smith<sup>3</sup>¶, Morgan Craig<sup>1,2, 4\*</sup>¶

4  
5 <sup>1</sup>CHU Sainte-Justine Research Centre, Montréal, Québec, Canada

6 <sup>2</sup>Department of Mathematics and Statistics, Université de Montréal, Montréal, Québec, Canada

7 <sup>3</sup>Department of Pediatrics, University of Tennessee Health Science Center, Memphis, Tennessee, USA

8 <sup>4</sup>Department of Physiology, McGill University, Montréal, Québec, Canada

9 <sup>5</sup>Department of Mathematics and Statistics, Concordia University, Montréal, Québec, Canada

10 <sup>6</sup>Department of Immunology, University of Pittsburgh, Pittsburgh, Pennsylvania, USA

11 <sup>7</sup>Natural Science Division, Pepperdine University, Malibu, California, USA

12  
13 ¶Co-senior authors

14 \*Corresponding author: [morgan.craig@umontreal.ca](mailto:morgan.craig@umontreal.ca)

15

16

17

18

19

20

21

22

23

24

25

26

27

28

29

30

31

32

33

34

35

36

37

## 38 Abstract

39 To understand the diversity of immune responses to SARS-CoV-2 and distinguish features that  
40 predispose individuals to severe COVID-19, we developed a mechanistic, within-host mathematical  
41 model and virtual patient cohort. Our results indicate that virtual patients with low production rates of  
42 infected cell derived IFN subsequently experienced highly inflammatory disease phenotypes, compared  
43 to those with early and robust IFN responses. In these *in silico* patients, the maximum concentration of  
44 IL-6 was also a major predictor of CD8<sup>+</sup> T cell depletion. Our analyses predicted that individuals with  
45 severe COVID-19 also have accelerated monocyte-to-macrophage differentiation that was mediated by  
46 increased IL-6 and reduced type I IFN signalling. Together, these findings identify biomarkers driving  
47 the development of severe COVID-19 and support early interventions aimed at reducing inflammation.

## 48 Author summary

49 Understanding of how the immune system responds to SARS-CoV-2 infections is critical for  
50 improving diagnostic and treatment approaches. Identifying which immune mechanisms lead to  
51 divergent outcomes can be clinically difficult, and experimental models and longitudinal data are only  
52 beginning to emerge. In response, we developed a mechanistic, mathematical and computational model  
53 of the immunopathology of COVID-19 calibrated to and validated against a broad set of experimental  
54 and clinical immunological data. To study the drivers of severe COVID-19, we used our model to  
55 expand a cohort of virtual patients, each with realistic disease dynamics. Our results identify key  
56 processes that regulate the immune response to SARS-CoV-2 infection in virtual patients and suggest  
57 viable therapeutic targets, underlining the importance of a rational approach to studying novel  
58 pathogens using intra-host models.

## 59 Introduction

60 Clinical manifestations of SARS-CoV-2 infection are heterogeneous, with a significant  
61 proportion of people experiencing asymptomatic or mild infections that do not require hospitalization.  
62 In severe cases, patients develop coronavirus disease (COVID-19) that may progress to acute  
63 respiratory distress syndrome (ARDS), which is frequently accompanied by a myriad of inflammatory  
64 indicators [1]. Mounting evidence points to a hyper-reactive and dysregulated inflammatory response  
65 characterized by overexpression of pro-inflammatory cytokines (cytokine storm) and severe  
66 immunopathology as specific presentations in severe COVID-19 [2–6]. An over-exuberant innate  
67 immune response with larger numbers of infiltrating neutrophils [7,8] arrests the adaptive immune  
68 response through the excessive release of reactive oxygen species that leads to extensive tissue damage  
69 and depletion of epithelial cells [9]. In addition, lymphopenia, in particular, is one of the most  
70 prominent markers of COVID-19 and has been observed in over 80% of patients [6, 10–12]. However,  
71 the immune mechanisms that lead to disparate outcomes during SARS-CoV-2 infection remain to be  
72 delineated.

73 Cytokines are critically important for controlling virus infections [13, 14] and are central to the  
74 pathophysiology of COVID-19, sometimes playing a detrimental role in the context of a cytokine storm

75 [10]. For example, interleukin-6 (IL-6) can stimulate CD8<sup>+</sup> T cell expansion under inflammatory  
76 conditions [15]; however, in hospitalized SARS-CoV-2 patients with lymphopenia, IL-6 has been  
77 shown to be elevated [16] without an increase in CD8<sup>+</sup> T cell counts [17]. Type I interferons (such as  
78 IFNs- $\alpha$ ,  $\beta$  [18]) also play a major role in limiting viral replication by inducing a refractory state in  
79 susceptible and infected cells [19–21]. Due to this, it has been suggested that a delay in mounting an  
80 effective IFN response may be responsible for COVID-19 severity [22] as it is for other highly  
81 pathogenic coronavirus (i.e. SARS-CoV and MERS) infections [13]. Overall, patients with severe  
82 COVID-19 present with lymphopenia [14, 23], and are likely to have increased inflammatory cytokines  
83 such as IL-6, granulocyte-macrophage colony-stimulating factor (GM-CSF), and granulocyte colony-  
84 stimulating factor (G-CSF) [7, 17, 24].

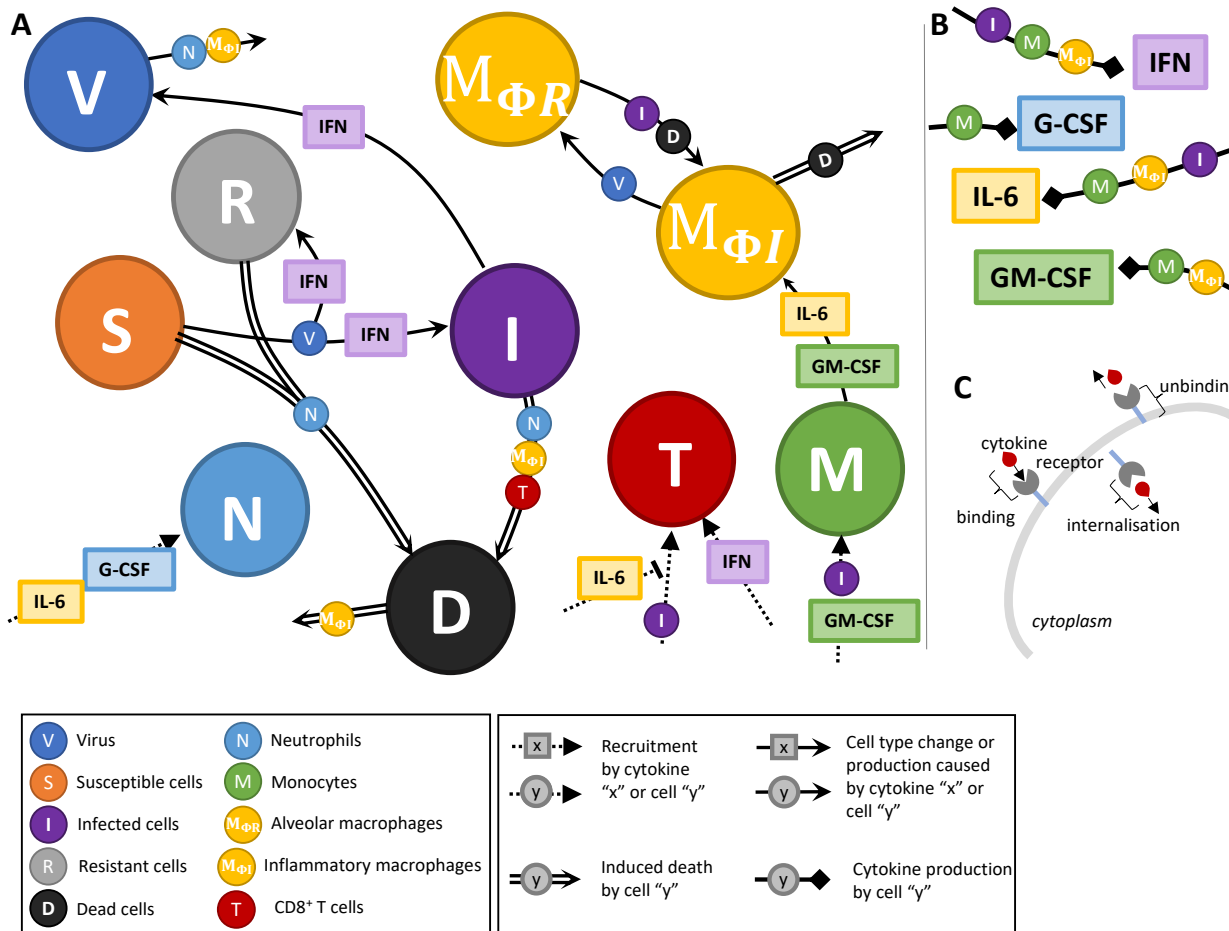
85 Because identifying which immune mechanisms lead to divergent outcomes can be difficult  
86 clinically, and experimental models and longitudinal data are only beginning to emerge, theoretical  
87 explorations are ideal [25]. Quantitative approaches combining mechanistic disease modelling and  
88 computational strategies are being increasingly leveraged to investigate inter- and intra-patient  
89 variability by, for example, developing virtual clinical trials [26–28]. More recently, viral dynamics  
90 models [29, 30] have been applied to understand SARS-CoV-2 within-host dynamics and their  
91 implications for therapy [31–36]. However, there are few comprehensive models that integrate detailed  
92 immune mechanisms and allow interrogation of the dynamics controlling divergent outcomes, and  
93 none have attempted to quantify the high degree of variability in patient responses to SARS-CoV-2  
94 through modelling.

95 In this study, we developed a mechanistic mathematical model to describe the within host  
96 immune response to SARS-CoV-2. We explicitly modelled the interactions between epithelial cells,  
97 innate and adaptive immune cells and cytokines. The model was fit to various *in vitro*, *in vivo*, and  
98 clinical data, analyzed to predict how early infection kinetics facilitate downstream disease dynamics,  
99 and used to create a virtual patient cohort with realistic disease courses. Our results suggest that mild  
100 and severe disease are distinguished by the rates of monocyte differentiation into macrophages and of  
101 IFN production by infected cells. In our virtual cohort, we found that severe COVID-19 responses were  
102 tightly correlated with a delay in the peak IFN concentration and that a large increase in IL-6 was the  
103 dominate predictor of CD8<sup>+</sup> T cell depletion in our virtual cohort. Importantly, these results provide  
104 insight into differential presentations of COVID-19 by identifying key regulators of severe disease  
105 manifestation particularly related to monocyte differentiation and IL-6 concentrations.

## 106 **Results**

107 **Modelling the immune response to SARS-CoV-2 and the impact of delayed IFN on infection**  
108 **dynamics**

109 To study the dynamics of SARS-CoV-2 infection and the development of COVID-19, we  
110 constructed a computational biology model of host-pathogen interactions (Eqs. S1-S22, with variables  
111 and parameters summarized in **Table S1** and schematic in **Figure 1**). The model includes susceptible  
112 lung epithelial cells ( $S$ ) that encounter virus ( $V$ ) and become infected ( $I$ ) before turning into damaged  
113 or dead cells ( $D$ ) due to viral infection or immune involvement. The immune response is orchestrated  
114 by a myriad of cytokines that act to stimulate the immune cell subsets present in the tissues and recruit  
115 cells from the bone marrow and circulation (**Figure 1A**). Upon infection, cells begin secreting type I  
116 IFNs ( $F$ ) that cause lung epithelial cells to become resistant to infection ( $R$ ) and decrease the  
117 production of newly infected cells [37]. Through stimulation by infected and dead cells, alveolar (lung  
118 tissue-resident) macrophages ( $M_{\phi R}$ ) become inflammatory macrophages, which also arise through  
119 macrophage ( $M$ ) differentiation by stimulation by GM-CSF ( $G$ ) or IL-6 ( $L$ ) [38]. Neutrophils ( $N$ ) are  
120 recruited to the infection site by G-CSF and release reactive oxygen species (ROS) causing bystander  
121 damage to infected and susceptible cells [39, 40]. CD8<sup>+</sup> T cells ( $T$ ) are subsequently recruited to the  
122 infection site following a delay to account for antigen presentation, with expansion modulated by type I  
123 IFN and IL-6 concentrations. See **Materials and Methods** for a complete description.

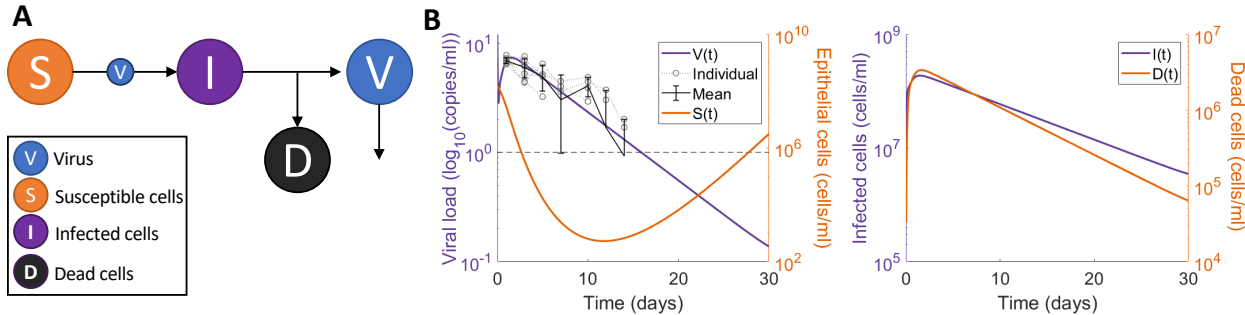


124

125 **Figure 1. Immune response to SARS-CoV-2 infection model schematic.** The model in Eqs. S1-S22 reduced  
126 to A) cell dynamics B) cytokine production dynamics and C) cytokine binding kinetics. Unique lines represent  
127 induced cell death (double line), recruitment (dashed line), cell type change or production (solid line), and  
128 cytokine production (square arrow). Cell and/or cytokines along joining lines denote a causal interaction. A)  
129 Virus (V) infects susceptible lung epithelial cells and creates either infected (I) or resistant (R) cells depending  
130 on the concentration of type I IFN. Infected cells then either die and produce new virus or are removed via  
131 inflammatory macrophages ( $M_{\phi I}$ ) or CD8<sup>+</sup> T cells (T) that induce apoptosis to create dead cells (D). Neutrophils  
132 (N) cause bystander damage (death) in all epithelial cells and are recruited by individually G-CSF and IL-6  
133 concentrations. CD8<sup>+</sup> T cells are recruited by infected cells and their population expands from IFN signalling. T  
134 cell recruitment is inhibited by IL-6 concentrations. Monocytes (M) are recruited by infected cells and GM-CSF  
135 and differentiate into inflammatory macrophages based on the individual concentrations of GM-CSF and IL-6.  
136 Tissue-resident macrophages ( $M_{\phi R}$ ) also become inflammatory macrophages through interaction with dead and  
137 infected cells. Dead cells are cleared up by inflammatory macrophages and also cause their death. B) Type I IFN  
138 is produced by infected cells, inflammatory macrophages and monocytes. G-CSF is produced solely by  
139 monocytes and GM-CSF is produced by monocytes and macrophages. IL-6 is produced by monocytes,  
140 inflammatory macrophages and infected cells. C) Cytokine receptor binding, internalization and unbinding  
141 kinetics considered for each cell-cytokine interaction.

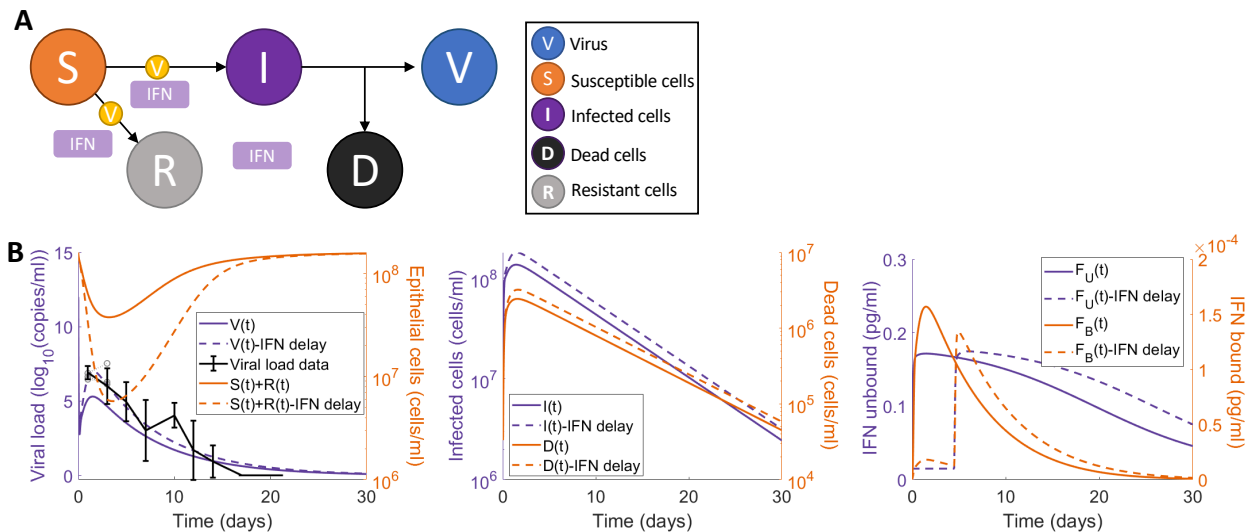
142 Because the model has several parameters that are undetermined biologically and insufficient  
143 data exists to confidently estimate their values, we used a stepwise approach to parameter estimation  
144 (see **Materials and Methods** and **Figures S1-S5**). We first confirmed that we could recapitulate early  
145 infection viral kinetics with a reduced version of the full model ('viral model'). For this, we excluded

146 immunological variables (i.e. only including **Eqs. 6-9**) and estimated parameters relating to viral  
147 kinetics by fitting to viral load data from macaques (see **Materials and Methods**). The resulting model  
148 dynamics were in good agreement to these early infection data (**Figure 2**) and demonstrate a rebound  
149 in epithelial lung tissue as the viral load and infected cells decrease.



150  
151 **Figure 2. Viral dynamics model fit to macaque viral data from Munster et al. [41]** A reduced version of the  
152 full model (all cytokine and immune cells set to 0, **Eqs. 6-9**) was fit to data from macaques [41] to estimate  
153 preliminary viral kinetic parameters. **A**) Virus ( $V$ ) infects susceptible cells ( $S$ ) making infected epithelial cells ( $I$ )  
154 which then die to produce dead cells ( $D$ ) and new virus. **B**) Comparison of predicted viral dynamics compared to  
155 observations from 6 animals, with susceptible cell kinetics (left) with predictions of infected and dead cells over  
156 time (right). We estimated  $\beta$ ,  $p$ ,  $d_I$ ,  $V_0$  and  $d_V$  from the reduced model in **A**) fit to data from Munster et al. [41]  
157 measuring the viral load in macaques after challenge with SARS-CoV-2 (**Table S1**).

158 We then isolated the IFN dynamics to assess clinical and experimental findings suggesting that  
159 delaying IFN results in more severe presentations in highly pathogenic coronavirus infections including  
160 SARS-CoV-2 [13, 14, 22]. Using the parameters obtained from the ‘viral model’ (**Eqs. 6-9; Table S1**),  
161 we then simulated the impact of IFN with the ‘IFN model’ (**Eqs. 10-16** and **Figure 3A**). We examined  
162 the predicted dynamics in response to delayed IFN by simulating with and without a fixed delay for  
163 IFN production from infected cells. Our results suggest that delaying type I IFN production by 5 days  
164 yields a 10-fold increase in tissue damage with only 20% of the lung tissue remaining on day 2 (**Figure**  
165 **3B**), caused by the increase in infected cells and subsequent lack of resistant cells. IFN dynamics were  
166 matched to systemic IFN- $\alpha$  concentrations from clinical cohorts by visual predictive check to confirm  
167 that predictions fell within the observed ranges [42] (**Figure S6A**).

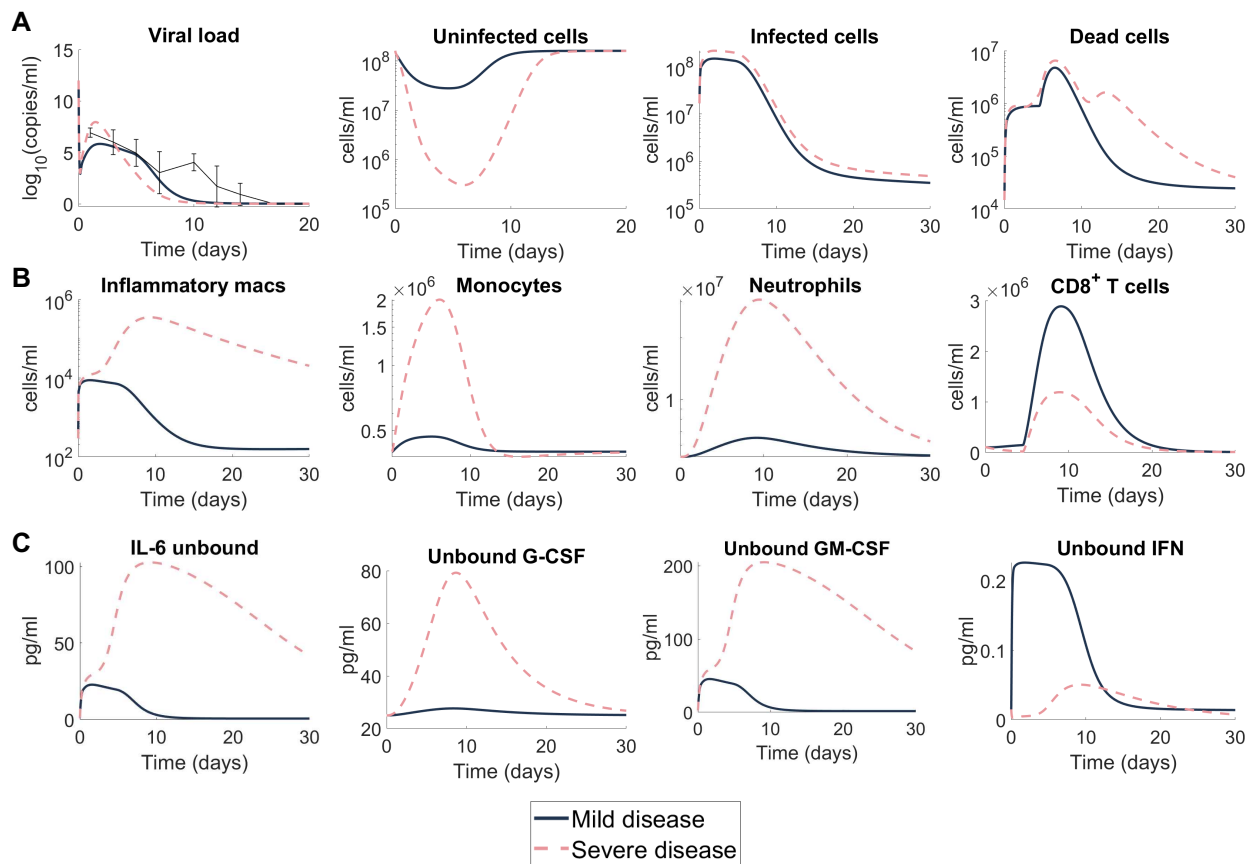


168

169 **Figure 3. Delayed type I IFN response impacts heavily on tissue survival in reduced model. A)** Submodel  
170 (Eqs. 10-16) with all non-IFN cytokines and immune cell interactions set to zero and only considering  
171 interactions between virus ( $V$ ) and susceptible ( $S$ ), infected ( $I$ ), resistant ( $R$ ), and dead ( $D$ ) epithelial cells. **B)**  
172 Predictions from the simplified model without delayed IFN production (solid lines) versus with a constant delay  
173 ( $\tau_F = 5$  days) (dotted lines). Solid black (left panel): viral loads from SARS-CoV-2 infection in macaques by  
174 Munster et al. [41] is overlayed with predicted viral dynamics.

175 **Immunologic determinants of mild and severe disease**

176 Next, to establish the mechanisms that differentiate mild versus severe disease, we simulated  
177 the full model (Eqs. S1-S22) using two different parameter sets. Mild disease dynamics were recreated  
178 using the estimated parameter values (Table S1) with the virus decay rate ( $d_V$ ) and the infected cell  
179 death rate ( $d_I$ ) recalculated to ensure that the maximum death rate of the virus and infected cells did not  
180 exceed the value obtained from the reduced viral dynamics model fit (Figure 2). Simulating mild  
181 disease, we predicted that all cell populations and cytokines rapidly return to homeostasis, with the  
182 immune response effectively clearing virus within 10 days (Figure 4 and Figure S7).  
183 Because severe SARS-CoV-2 infection results in lower levels of IFN [42] and increased monocytes  
184 [43], we recapitulated severe disease by modulating model parameters relating to these processes, i.e.,  
185 the rates of IFN production from infected cells and macrophages were decreased, and the rate of  
186 monocyte recruitment from the bone marrow by infected cells was increased. With these changes, the  
187 model predicted a dramatic shift in disease response that was characterized by a cytokine storm  
188 (elevated IL-6, GM-CSF and G-CSF), high ratios of innate to adaptive immune cells, and a marked  
189 reduction in healthy viable lung tissue (Figure 4A), whereas changes in viral load remained relatively  
190 consistent with mild disease.



191

192 **Figure 4. Predicting mild and severe COVID-19 dynamics.** Mild disease (solid lines) dynamics obtained by  
193 using baseline parameter estimates (Tables S1) while severe disease dynamics (dashed lines) were obtained by  
194 decreasing the production rate of type I IFN ( $p_{I,1}$ ) and increasing the production of monocytes ( $p_{M,1}$ ) and their  
195 differentiation to macrophages ( $\eta_{F,M\Phi}$ ). **A**) Viral load and lung cells concentrations (susceptible, resistant,  
196 infected, and dead cells). Solid black line with error bars indicates macaque data [41] (see **Figure 2**). **B**) Immune  
197 cell concentrations (inflammatory macrophages, monocytes, neutrophils, and CD8<sup>+</sup> T cells). **C**) Unbound  
198 cytokine concentrations (free IL-6, GM-CSF, G-CSF, and type I IFN). Time evolution of all model variables is  
199 shown in **Figure S7** (including bound cytokine and alveolar macrophages).

200 In addition, there was a significant increase in the number of inflammatory macrophages  
201 (**Figure 4B**), IL-6, GM-CSF and, importantly, a delayed and reduced IFN peak (**Figure 4C**). In  
202 comparison to the mild disease, inflammatory macrophages and neutrophils (**Figure 4B**) remained  
203 elevated for at least 30 days after initial infection. Comparing mild and severe disease highlighted  
204 significant differences in the area under the curve (AUC) of macrophages ( $6 \times 10^4$  cells/ml versus  
205  $3 \times 10^{11}$  cells/ml) and neutrophils ( $2 \times 10^8$  cells/ml versus  $3 \times 10^{13}$  cells/ml) over 30 days.

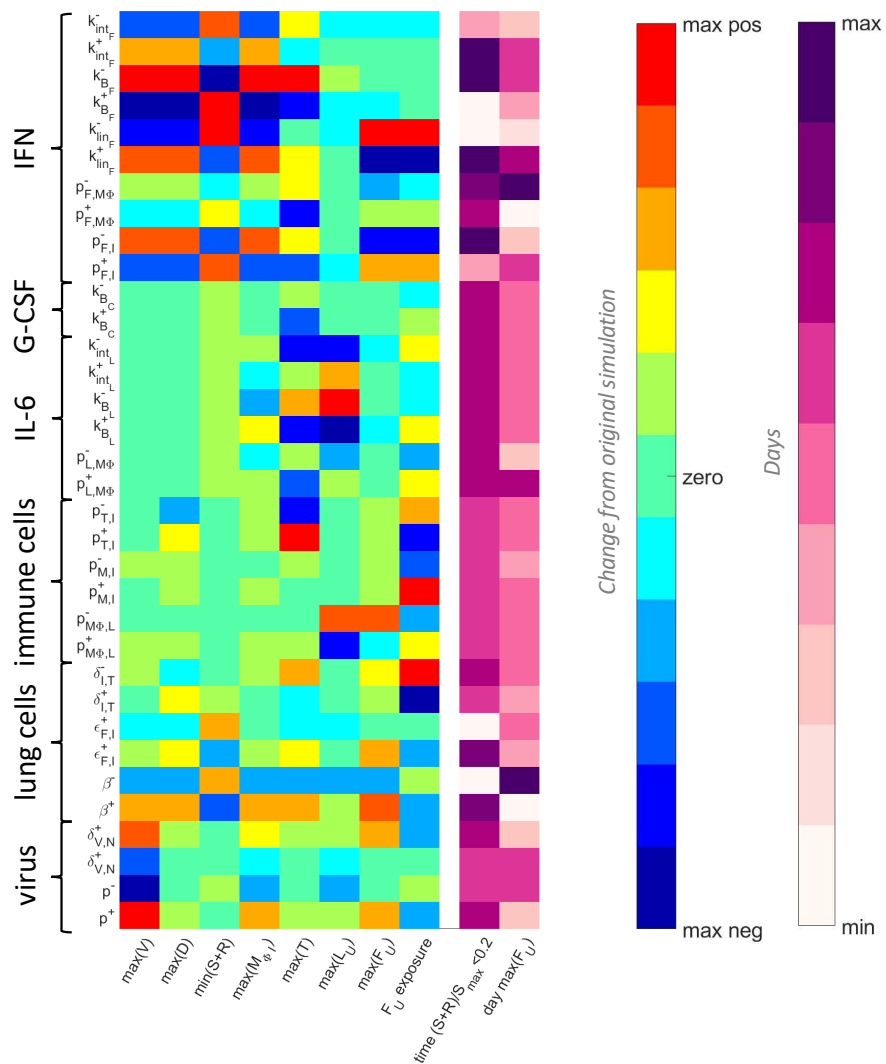
206 Interestingly, inflammation remained high in the severe disease scenario despite the virus being  
207 cleared slightly faster ( $\sim 1$  day) than in the case of mild disease (**Figure 4A**). Further, the peak of  
208 inflammatory macrophages increased from  $\sim 10^4$  cells/ml to  $\sim 10^6$  cells/ml in severe scenarios  
209 compared to mild scenarios (**Figure 4B**). The model also accurately predicted that CD8<sup>+</sup> T cell  
210 dynamics were lower in severe cases, which is indicative of lymphopenia and similar to clinical

211 observations from patients with severe COVID-19 [14, 23]. Despite varying only three parameters to  
212 generate disparate dynamics, the immune cell and cytokine dynamics were qualitatively in line with  
213 clinical observations for IFN- $\alpha$  [42], IL-6 [42, 44], and G-CSF [24] (**Figure S6B-F**).

214 **Macrophages, CD8<sup>+</sup> T cells, IFN and IL-6 regulates response to SARS-CoV-2 infection**

215 To further understand how the host immune system regulates the response to SARS-CoV-2  
216 infection, we conducted a local sensitivity analysis by varying each parameter individually by  $\pm 20\%$   
217 and comparing a set of metrics (see **Materials and Methods**) chosen to provide a comprehensive  
218 understanding of each parameter's impact on the host-pathogen dynamics. This analysis identified 17  
219 sensitive parameters (**Figure 5**) relating to virus productivity ( $p, \delta_{V,N}, \beta, \epsilon_{F,I}$ ), CD8<sup>+</sup> T cell induced  
220 epithelial cell apoptosis ( $\delta_{I,T}$ ), macrophages, monocyte and CD8<sup>+</sup> T cell production ( $p_{M\Phi,I,L}, p_{M,I}, p_{T,I}$ ),  
221 IL-6 ( $p_{L,M\Phi}, k_{B_L}, k_{int_L}$ ), G-CSF ( $k_{B_C}$ ), and IFN ( $p_{F,I}, p_{F,M\Phi}, k_{lin_F}, k_{B_F}, k_{int_F}$ ).

222 The rate of viral infectivity ( $\beta$ ) had a particularly significant impact on all metrics where  
223 increases resulted in higher viral loads and longer periods of tissue damage  $> 80\%$ . The duration of  
224 extensive tissue damage ( $> 80\%$  damaged) also increased with IFN potency ( $\epsilon_{F,I}$ ). Decreasing the rate  
225 of IL-6-induced monocyte differentiation into inflammatory macrophages ( $p_{M\Phi,L}$ ) increased the peak of  
226 both IL-6 and IFN. Notably, changes to parameters that increased the bound IFN concentration, i.e.  
227 increasing the binding and production rates ( $k_{B_F}$  and  $p_{F,I}$ ) and decreasing the internalization and  
228 clearance rates ( $k_{lin_F}$  and  $k_{int_F}$ ) induced significant changes in most metrics (**Figure 5**). See **Figure S8**  
229 for complete sensitivity analysis results.



230 **Figure 5. Parameters driving COVID-19 severity.** A local sensitivity analysis was performed by varying each  
 231 parameter  $\pm 20\%$  from its originally estimated value and simulating the model. Predictions were then compared  
 232 to baseline considering: Maximum viral load ( $\max(V)$ ), maximum concentration of dead cells ( $\max(D)$ ),  
 233 minimum uninfected live cells ( $\min(S+R)$ ), maximum concentration of inflammatory macrophages ( $\max(M_{\phi I})$ ),  
 234 maximum number of CD8<sup>+</sup> T cells ( $\max(T)$ ), maximum concentration of IL-6 ( $\max(L_U)$ ), maximum  
 235 concentration of type I IFN ( $\max(F_U)$ ), the total exposure to type I IFN ( $F_U$  exposure), the number of days  
 236 damaged tissue was  $>80\%$  ( $\text{time}(S+R)/S_{max}$ ), and the day type I IFN reached its maximum (day  $\max(F_U)$ ).  
 237 The heatmaps show the magnitude change of each metric, where blue signifies the minimum value observed and  
 238 red signifies the maximum value observed, or by the number of days, where light to dark pink signifying  
 239 increasing number of days from zero. The most sensitive parameters are shown here (for complete parameter  
 240 sensitivity results, see **Figure S8**).

241 **Virtual patient cohort identifies heterogeneity in immune dynamics and severity**

242 To better understand the clinical variability in SARS-CoV-2 infection severity [1], we next  
 243 generated a cohort of 200 virtual patients (see **Materials and Methods** and **Figure 7**). To create each  
 244 *in silico* patient, seven patient-specific parameters were sampled from normal distributions with means  
 245 corresponding to their respective fixed values and standard deviations inferred from clinical  
 246 observations (**Table 1**). In doing this, we assumed intrinsic interindividual heterogeneity in monocyte

247 to macrophage differentiation, production of IL-6 by macrophages, recruitment of macrophages by the  
248 presence of infected cells, and production of IFN by infected cells, macrophages and monocytes,  
249 respectively.

250 Parameters were chosen based on their impact on maximum IL-6 and IFN levels as well as  
251 tissue damage observed in the sensitivity analysis ( $p_{M\Phi_{I,L}}$ ,  $p_{L,M\Phi}$ ,  $p_{F,I}$ ,  $p_{M,I}$ , and  $\epsilon_{F,I}$ ; **Figure 5**). In  
252 addition, we designated patient-specific parameters accounting for alternate pathways through which  
253 IFN is affected by innate immune cells ( $\eta_{F,M\Phi}$  and  $p_{F,M}$ ). For the production of IL-6 by macrophages  
254 and monocyte to macrophage differentiation via IL-6 stimulation, standard deviations were inferred  
255 from IL-6 levels in non-mechanically ventilated patients (mild) and from mechanically ventilated  
256 patients (severe) [44] (**Figure S7D**). Standard deviations for the production of IFN by infected cells  
257 were determined from the 95% confidence interval for IFN- $\alpha$  from Trouillet-Assant et al. [42] (**Figure**  
258 **S7A-B**), and, lastly, the standard deviation for the production of IFN by macrophages was obtained  
259 from the 95% confidence interval in Sheahan et al. [45]. The variation in virtual patient responses was  
260 then constrained by experimental and clinical viral loads, IFN, neutrophil, IL-6, and G-CSF (**Figure 7**).  
261 The resulting cohort dynamics were within ranges for IFN and IL-6 measurements in asymptomatic to  
262 severe COVID-19 patients in the literature [11, 17] (**Figure S9**).

Param	Units	Description	Mean	Ref	Std Dev	Ref	Range
$p_{M\Phi_{I,L}}$	1/day	Monocyte to macrophage differentiation by IL-6	1.7	[46]	2.2	[7]	[0, 9.9]
$p_{L,M\Phi}$	pg/ml/day	IL-6 production by activated macrophages	1872	[47]	2.2	[7]	[1863, 1880]
$p_{F,I}$	pg/ml/day	IFN production by infected cells	2.82	[48]	1.9	[44]	[0, 12.2]
$p_{M,I}$	1/day	Monocyte recruitment rate by infected cells	0.22	[49]	0.08	[50]	[0, 0.63]
$\eta_{F,M\Phi}$	$10^9$ cells/ml	IFN by infected cells	0.001 <sub>2</sub>	[48]	$10^{-5}$	[51]	[0, $10^{-4}$ ]
$\epsilon_{F,I}$	pg/ml	IFN production of CD8 <sup>+</sup> T cells	0.004	[52]	$10^{-5}$	[45]	[0, $10^{-4}$ ]
$p_{F,M}$	pg/ml/day	IFN production by monocytes	3.56	[53, 54]	0.013	[53]	[3.4, 3.6]

263 **Table 1 Virtual patient-specific parameter values.** Seven parameters in the model were deemed patient-  
264 specific and were drawn from a normal distribution with mean the parameter value obtained either through  
265 fitting or from the literature (**Table S1**). The standard deviation (Std Dev) for each normal distribution was  
266 informed by values in the literature (see **Materials and Methods** and Supplementary Information Sections  
267 S6.1). Initial parameter sampling and new parameters generated through the simulated annealing optimization,  
268 were bounded within the interval range noted. All other parameters in the model were fixed to their original  
269 value (**Table S1**).

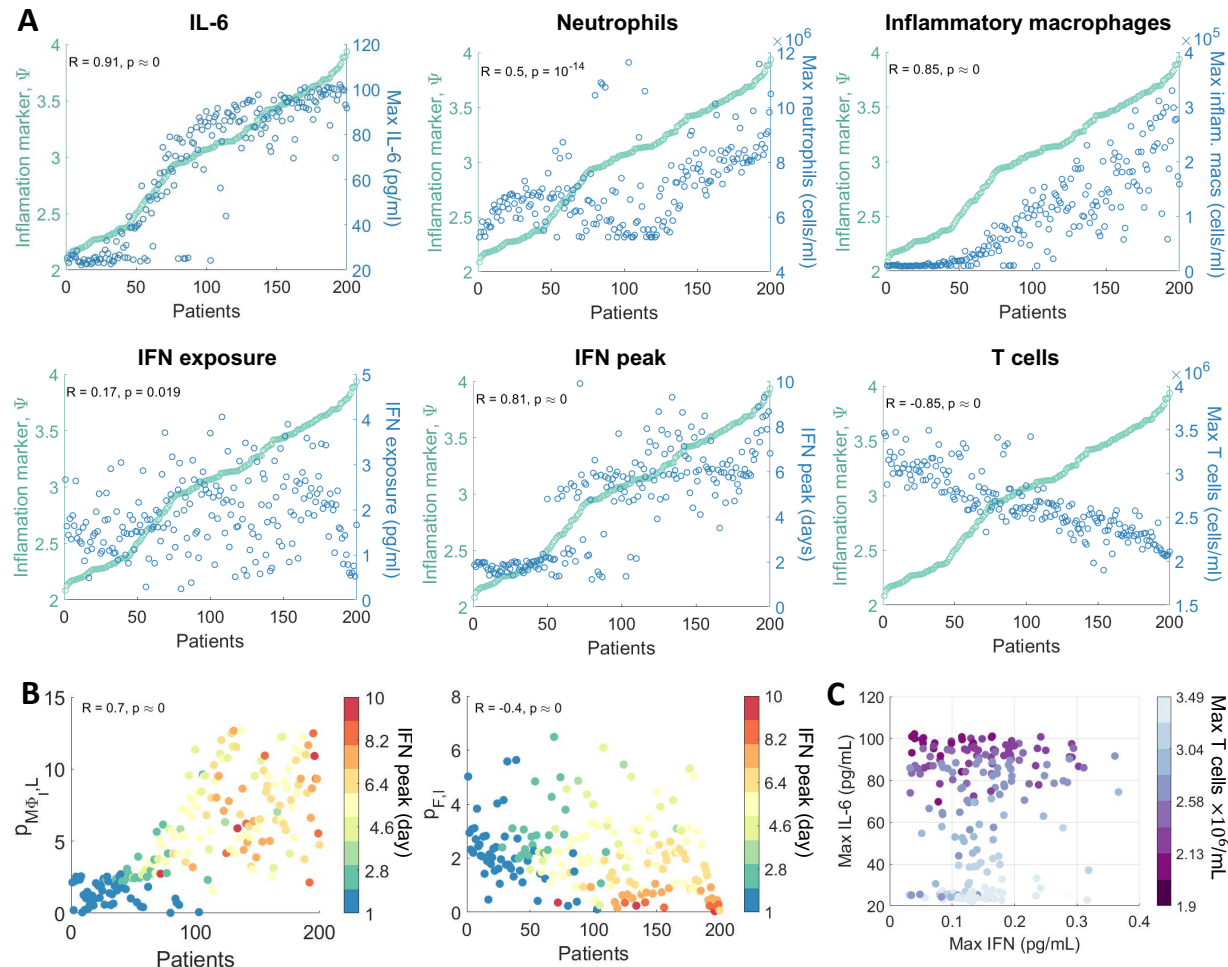
270 To quantify disease severity, we introduced an inflammation variable,  $\Psi$ , that measured  
271 maximum IL-6, neutrophils and tissue damage (Eq. 18) and then compared it to individual  
272 characteristics of each virtual patient's disease. We evaluated each virtual patient's maximum IL-6,  
273 CD8<sup>+</sup> T cells, and neutrophils; minimum percentage of healthy lung tissue; the time to peak IFN; and  
274 total IFN exposure (area under the curve or AUC) within 21 days of infection. Ordering patients by  
275 their value of  $\Psi$  and plotting the corresponding values for different characteristics evaluated showed a  
276 clear separation between those with mild disease and those with severe disease (Figure 6A).

277 Patients with higher inflammation had higher IL-6, neutrophil, and inflammatory macrophage  
278 concentrations (Figure 6A). While the IFN exposure was not significantly stratified by  $\Psi$ , the peak of  
279 IFN and CD8<sup>+</sup> T cell levels were strongly negatively correlated with the inflammation marker ( $R =$   
280  $-0.85$ ,  $p < 1 \times 10^{-9}$ , see Materials and Methods). IL-6 was most noticeably correlated with  $\Psi$  ( $R =$   
281  $0.91$ ,  $p < 1 \times 10^{-9}$ ), with a distinct upper bound in the concentration ( $\sim 100$  pg/ml) achieved in 50% of  
282 the virtual cohort. There appeared to be a transition phase in inflammation driven by neutrophil levels  
283 where patients with moderate inflammation ( $3 < \Psi < 3.5$ ) had low counts (less than  $7 \times 10^6$  cells/ml)  
284 compared to patients with more severe inflammation ( $\Psi \geq 3.5$ ) who had higher levels ( $p =$   
285  $1.46 \times 10^{-6}$ ). Despite this, patients with moderate inflammation exhibited increased disease markers  
286 including delayed IFN peaks and lower CD8<sup>+</sup> T cells, compared to patients with mild inflammation  
287 ( $\Psi \leq 3$ ).

288 A distinct jump in the timing of the IFN peak in the virtual cohort ( $p < 1 \times 10^{-5}$ ) was  
289 correlated with inflammation, as patients with low inflammation ( $\Psi \leq 3$ ) had peaks at day 2 compared  
290 to day 6 in patients with higher inflammation ( $\Psi > 3$ ). Grouping virtual individuals by their time to IFN  
291 peak suggests that those with IFN peaks after day 3 of infection also had fewer macrophages ( $p <$   
292  $1 \times 10^{-5}$ ) and larger numbers of CD8<sup>+</sup> T cells ( $p < 1 \times 10^{-5}$ ). Overall, delays in IFN peak did not  
293 cause significant changes to viral load but were sufficient to cause major tissue damage (100x  
294 reduction in viable tissue remaining) and over-heightened immune responses (4x increase in maximum  
295 IL-6 and GM-CSF concentrations).

296 We found a positive correlation ( $R = 0.67$ ,  $p = 1.58 \times 10^{-8}$ ) between the time to peak IFN  
297 concentration for each patient against their IFN production rate from infected cells (Figure 6B).  
298 Interestingly, the time to peak IFN for each patient was also strongly related to their rate of IL-6-  
299 stimulated monocyte differentiation into macrophages. Low IFN production rates were predominately  
300 responsible for significantly delayed IFN peaks over 6 days after infection, whereas IFN peaks within 3  
301 days of infection were largely caused by lower rates of monocyte to macrophage differentiation.

302 Further, examining the relationship between each virtual patient's maximum IL-6, IFN, and CD8<sup>+</sup> T  
 303 cell concentrations (**Figure 6C**) identified a weaker correlation between the maximum concentration of  
 304 CD8<sup>+</sup> T cells and IFN ( $R = 0.24$ ,  $p = 0.0008$ ) as opposed to with IL-6 ( $R = -0.86$ ,  $p < 1 \times 10^{-9}$ ).



305  
 306 **Figure 6. Virtual Cohort of SARS-CoV-2 infected patients.** 200 virtual patients were generated by sampling  
 307 parameters related to macrophage, IL-6, and IFN production ( $p_{M\Phi_I,L}$ ,  $p_{L,M\Phi}$ ,  $p_{F,I}$ ,  $p_{M,I}$ ,  $\eta_{F,M\Phi}$ ,  $\epsilon_{F,I}$ , and  $p_{F,M}$ ) from  
 308 normal distributions with mean equal to their original values and standard deviation inferred from clinical  
 309 observations (**Figure 7**). Each virtual patient had a distinct parameter set that was optimized to that patient's  
 310 dynamics in response to SARS-CoV-2 infection corresponded to physiological intervals reported in the literature  
 311 (see **Materials and Methods**). **A**) Infection and immune response metrics (blue) in individual patients were  
 312 compared to inflammatory variable  $\Psi$  (green). Each point represents an individual patient, ordered according to  
 313  $\Psi$ . The correlation coefficient ( $R$ ) and p-value are indicated for each, with  $\alpha < 0.05$  denoting significant  
 314 correlations. **B**) Parameters most correlated to the IFN peak time were the rates of macrophage production via  
 315 IL-6 ( $p_{M\Phi_I,L}$ ) and the IFN production by infected cells ( $p_{F,I}$ ). Individual patient values for these parameters are  
 316 plotted as circles coloured by the patient's corresponding day of IFN peak (see color bar). Patients are ordered  
 317 by their inflammation marker  $\Psi$ . **C**) Correlations between maximal IFN, IL-6, and T cell concentrations for each  
 318 patient (circles). Circle colour corresponds to the maximal T cell concentration of each patient.

## 319 Discussion

320 Serial immunological measurements from COVID-19 patients are only beginning to be  
 321 collected, and the ability to assess initial infection kinetics and the drivers of the ensuing disease

322 remains limited. The data-driven mechanistic mathematical model and virtual patient cohort developed  
323 here identified important immunological drivers of COVID-19. In particular, to recreate severe  
324 dynamics, it was sufficient to vary only two processes in the model: the rates of type I IFN production  
325 from infected cells and macrophages, and the rate of monocyte recruitment by infected cells. This  
326 suggests that the distinction between severe and mild disease may be driven by a limited set of causal  
327 regulators. The effect on IFN production may be further exacerbated by autoimmunity against type I  
328 IFNs, which has been shown to correlate to life-threatening COVID-19 pneumonia in 2.6% of women  
329 and 12.5% of men [18].

330 Our results show that delaying type I IFN production is sufficient to cause major tissue damage  
331 and heightened immune responses yet have little impact on peak viral loads. In the severe disease  
332 simulation, viral load was cleared marginally faster (~1 day) in comparison to the mild disease  
333 simulation. This finding is supported by recent clinical evidence showing that an increased rate of viral  
334 decline rather than peak viral load may be more predictive of disease severity [6]. This therefore  
335 suggests that viral load may not be a necessary attribute to obtain severe tissue damage. Instead, our  
336 model predicts that increases in tissue damage occur through heightened innate immune responses.  
337 Evaluating SARS-CoV-2 infection in a cohort of 200 virtual patients revealed several immunological  
338 responses responsible for differential disease presentation. Notably, a distinct, emergent switch in the  
339 type I IFN response corresponded with late IFN peaks and more severe disease (i.e., higher  
340 inflammation  $\Psi$ ). This supports previous findings that connect a delay in type I IFN with more severe  
341 presentations of highly pathogenic coronaviruses infections including SARS-CoV, MERS-CoV, and  
342 SARS-CoV-2 [13, 14, 22]. Virtual patients with rates of monocyte differentiation close to the rate at  
343 homeostasis tended to achieve peak IFN concentrations approximately 2 days after infection compared  
344 to those with higher inflammation and later IFN responses, who had at least a 3-fold increase in this  
345 rate. This switch in timing was caused by increased rates of monocyte-to-macrophage differentiation  
346 and decreased production of IFN by infected cells, with the initial delay of IFN caused by increased  
347 monocyte differentiation and the more extreme IFN delays caused by IFN production from infected  
348 cells, indicating that the timing of the IFN peak in a patient may allow for improved stratification into  
349 treatment arms designed to target one or both of these responses. The finding that IFN binding was  
350 predictive of the duration of lung tissue damage, suggests that virus-intrinsic properties and their ability  
351 to inhibit receptor mediated binding and endocytosis could delay IFN production and cause  
352 downstream increases in IL-6 and GM-CSF resulting in severe disease. Our results further highlight  
353 that lymphopenia is tightly correlated with maximum IL-6 concentration and less dependent on the  
354 timing of IFN.

355 The ability of our model to recapitulate severe disease by, in part, regulating monocyte  
356 differentiation raises the possibility that patients with low monocyte levels [7] may benefit from  
357 treatments that better regulate monocyte differentiation. This is in line with recent studies identifying  
358 distinct transcriptional factors as regulators of differentiated monocyte fates in inflammatory conditions  
359 [55, 56]. It also raises the possibility that modulation by exogenous cytokines, including macrophage  
360 colony-stimulating factor in combination with IL-4 and tumour necrosis factor-alpha (TNF- $\alpha$ ), may be  
361 able to direct monocyte differentiation in favour of monocyte-derived dendritic cells and reduce this  
362 response [55]. Recently, the neutralization of both TNF- $\alpha$  and IFN- $\gamma$  has been found to benefit patients  
363 with COVID-19 or other cytokine storm-drive syndromes by limiting inflammation and tissue damage  
364 [57]. Given that TNF- $\alpha$  also has a secondary benefit on monocyte differentiation, our results support  
365 the viability of this avenue of treatment. Caution should be noted, however, given that previous  
366 attempts to regulate host responses by IL-6 blockade have proven unsuccessful [58].

367 Together, our findings support the idea that early interventions aimed at reducing inflammation  
368 are more likely to be beneficial for patients at risk of progressing to severe COVID-19 than attempts to  
369 inhibit cytokine storm later in the disease course, given that early IFN responses were found to provoke  
370 better controlled immune responses and outcomes in our virtual cohort. It will be essential to  
371 characterize both the timing and mechanisms of proposed therapeutic interventions to develop effective  
372 treatments to mitigate severe disease.

## 373 Materials and Methods

### 374 Mathematical model of the immune response to SARS-CoV-2

375 Our model was developed to examine SARS-CoV-2 infection dynamics and identify  
376 immunological drivers of disease severity (**Eqs. S1-S22**). Throughout, cytokine and immune cell  
377 interactions and effects were described by Hill functions as

$$\frac{B^h}{B^h + \gamma^h}, \quad 1$$

378 where  $B$  is the interacting compound,  $\gamma$  its half-effect value, and  $h$  the Hill coefficient [59, 60]. Further,  
379 for a given cytokine  $X$  and cell population  $Y$ , the production (recruitment/differentiation) rate of  $X$  by  $Y$   
380 was denoted by  $p_{X,Y}$  and the rate of production of  $Y$  by  $X$  by  $p_{Y,X}$ . The half-effect concentration (i.e.  $\gamma$   
381 in **Eq. 1**) of cytokine  $X$  on cell population  $Y$  was represented by  $\epsilon_{X,Y}$  and the half-effect concentration  
382 of cell  $Y$  affecting cytokine  $X$  was given by  $\eta_{X,Y}$ . The natural death rate of cell  $Y$  was denoted by  $d_Y$ ,  
383 and the rate of induced death of cell  $Y$  by cell  $Z$  by  $\delta_{Y,Z}$ . Lastly, the carrying capacity concentration of  
384 cell  $Y$  was denoted by  $Y_{max}$ , and regeneration or proliferation rates by  $\lambda_Y$ .

385 We modelled virus ( $V$ ) being produced by infected cells at rate  $p$  and cleared via exponential  
386 clearance at rate  $d_V$ , which accounts for all contributions to viral degradation except macrophage- and  
387 neutrophil-mediated clearance. Immune-mediated viral clearance via phagocytosis by inflammatory  
388 macrophages [61] and neutrophil extracellular traps (NETs—extracellular chromatin fibres produced  
389 by neutrophils to control infections) [39, 40] was considered to occur at rates  $\delta_{V,M\Phi_I}$  and  $\delta_{V,N}$ ,  
390 respectively. Susceptible epithelial cells ( $S$ ) grow logistically with per capita proliferation rate  $\lambda_S$  and  
391 carrying capacity  $S_{max}$ , and become infected ( $I$ ) at rate  $\beta$ . The damage inflicted on epithelial cells by  
392 neutrophils was modelled using a Hill function (Eq. 1) [60], where neutrophils kill/damage epithelial  
393 cells at rate  $\delta_N$  through the release of NETs and other antimicrobials proteins [39, 40]. The constant  $\rho$   
394 ( $0 < \rho < 1$ ) was included to modulate bystander damage of uninfected cells ( $S$  and  $R$ ).

395 For the purposes of our investigation, we only considered type I IFN dynamics (primarily IFN-  
396  $\alpha, \beta$ ). Type I IFN ( $F_U$  and  $F_B$ ) reduces the infectivity and replication capability of viruses by stimulating  
397 cells to become resistant to infection. These resistant cells ( $R$ ) proliferate at a rate equivalent to  
398 susceptible cells ( $\lambda_S$ ). The concentration of bound IFN ( $F_B$ ) modulates the creation of infected and  
399 resistant cells [19, 21, 62, 63], where increasing the concentration of IFN causes more cells to become  
400 resistant to infection and less to become productively infected ( $I$ ). The potency of this effect is  
401 controlled by the half-effect parameter  $\epsilon_{F,I}$ . Following the eclipse phase (which lasts  $\tau_I$  hours),  
402 productively infected cells ( $I$ ) produce virus before undergoing virus-mediated lysis at rate  $d_I$ .  
403 Although various immune cell subsets contribute to infected cell clearance, we limited our  
404 investigation to macrophages and effector CD8 $^+$  T cells which induce apoptosis at rates  $\delta_{I,M\Phi}$  and  $\delta_{I,T}$ ,  
405 respectively.

406 The accumulation of dead cells ( $D$ ) was assumed to occur through infected cell lysis  $d_I$ ,  
407 neutrophil damage/killing of epithelial cells  $\delta_N$ , macrophage phagocytosis of infected cells  $\delta_{I,M\Phi}$ ,  
408 macrophage exhaustion  $\delta_{M\Phi,D}$ , and CD8 $^+$  T cell killing of infected cells  $\delta_{I,T}$ . These dead cells  
409 disintegrate relatively quickly [64] at rate  $d_D$ , and are cleared through phagocytosis by macrophages  
410 [65] at rate  $\delta_{D,M\Phi}$ .

411 Resident alveolar macrophages ( $M_{\Phi_R}$ ) are replenished at a logistic rate inversely proportion to  
412 viral load with maximal rate of  $\lambda_{M\Phi}$  and half-effect  $\epsilon_{V,M\Phi}$  (i.e. as the virus is cleared, the inflammatory  
413 macrophage pool replenishes the alveolar macrophage population in the lung). We modelled the  
414 transition of alveolar macrophages to inflammatory macrophages ( $M_{\Phi_I}$ ) as dependent on infected and  
415 dead cells, with a maximal rate of  $\alpha_{I,M\Phi}$ . Resident macrophages die naturally at a rate  $d_{M\Phi_R}$  or due to  
416 the clearing of dead cells (exhaustion) [65] at rate  $\delta_{M\Phi,D}$ .

417 Inflammatory macrophages are produced by three distinct pathways (acting individually or in  
418 concert): 1) stimulated tissue-resident macrophages  $a_{I,M\Phi}$ , (2) GM-CSF-dependent monocyte  
419 differentiation, with maximal production  $p_{M,G}$  and half effect  $\epsilon_{G,M}$ , and (3) IL-6-dependent monocyte  
420 differentiation, with maximal production rate  $p_{M\Phi_{I,L}}$  and half-effect  $\epsilon_{L,M\Phi_I}$ . We assumed that  
421 inflammatory macrophages die naturally at rate  $d_{M\Phi_I}$  or from clearing dead cells at a rate  $\delta_{M\Phi,D}$ .

422 We have previously shown that endogenous cytokine concentrations are far from quasi-  
423 equilibrium at homeostasis [66]. Therefore, to describe the pharmacokinetics and pharmacodynamics  
424 of cytokine binding and unbinding, we leveraged the framework established in Craig et al. [66] (**Figure**  
425 **1C**) for IFN ( $F_B$  and  $F_U$ ), IL-6 ( $L_B$  and  $L_U$ ), GM-CSF ( $G_B$  and  $G_U$ ), and G-CSF ( $C_B$  and  $C_U$ ). In its  
426 general form, this pharmacokinetic relationship is expressed as

$$\frac{dY_U}{dt} = Y_{prod} - k_{lin}Y_U - k_B(XA - Y_B)(Y_U)^{POW} + k_U Y_B, \quad 2$$

$$\frac{dY_B}{dt} = -k_{int}Y_B + k_B(XA - Y_B)(Y_U)^{POW} - k_U Y_B \quad 3$$

427 where  $Y_U$  and  $Y_B$  are free and bound cytokines,  $Y_{prod}$  is the rate of endogenous cytokine production,  $k_B$   
428 and  $k_U$  are the respective binding and unbinding rates,  $k_{int}$  is the internalization rate of bound cytokine,  
429 and  $k_{lin}$  is the elimination rate. Here,  $POW$  is a stoichiometric constant,  $A$  is a scaling factor and  $X$  is  
430 the sum of all cells modulated by the cytokine with

$$XA = \hat{p}Y_{MW}K10^nX. \quad 4$$

431 where  $\hat{p}$  is a constant relating the stoichiometry between cytokine molecules and their receptors,  $K$  is  
432 the number of receptors specific to each cytokine on a cell's surface and  $10^n$  is a factor correcting for  
433 cellular units (see **Eqs. S19-S22**). The molecular weight was calculated in the standard way by dividing  
434 the cytokine's molar mass ( $MM$ ) by Avogadro's number ( $Y_{MW} = MM/6.02214 \times 10^{23}$ ).

435 We considered unbound IL-6 ( $L_U$ ) to be produced from productively infected cells,  
436 inflammatory macrophages, and monocytes, with bound IL-6 ( $L_B$ ) resulting from binding to receptors  
437 on the surface of neutrophils, CD8<sup>+</sup> T cells and monocytes. Unbound GM-CSF ( $G_U$ ) was assumed to be  
438 produced from inflammatory macrophages and monocytes and bind to receptors on monocytes to  
439 create bound GM-CSF ( $G_B$ ). GM-CSF can be produced by CD8<sup>+</sup> T cells [67], but this was excluded  
440 because it was insignificant to the full system's dynamics. Unbound G-CSF ( $C_U$ ) is secreted by  
441 monocytes, with bound G-CSF ( $C_B$ ) produced via binding to neutrophil receptors. Lastly, because  
442 unbound type I IFNs ( $F_U$ ) are known to be produced by multiple cell types in response to viral  
443 infection, including lymphocytes, macrophages, endothelial cells and fibroblasts [62], we modelled its

444 unbound production from infected cells, infiltrating/inflammatory macrophages, and monocytes, and its  
 445 binding to receptors on both CD8<sup>+</sup> T cells and infected cells (**Figure 1B**).

446 The pharmacokinetics and pharmacodynamics of G-CSF on neutrophils ( $N$ ) were taken directly  
 447 from Craig et al. [66]:

$$\frac{dN}{dt} = \left( N_{prod}^* + (\psi_N^{max} - N_{prod}^*) \frac{C_{BF} - C_{BF}^*}{C_{BF} - C_{BF}^* + \epsilon_{C,N}} \right) N_R. \quad 5$$

448 Neutrophil recruitment of bone marrow reservoir neutrophils ( $N_R$ ) was modelled to occur via the bound  
 449 fraction of G-CSF [68] ( $C_{BF} = C_B(t)/(A_c N(t))$ ) at rate  $N_{prod}^*$  which increases towards its maximal  
 450 value  $\psi_N^{max}$  as a function of increasing G-CSF. During the acute phase of inflammation, endothelial  
 451 cells produce IL-6 leading to the attraction of neutrophils [69]. This was modelled as recruitment with  
 452 maximal rate  $p_{N,L}$  and half-effect parameter  $\epsilon_{D,L}$ . Neutrophils die at rate  $d_N$ .

453 Monocytes ( $M$ ) are recruited by bound GM-CSF [70], similar to neutrophils (**Eq. 5**), with bone  
 454 marrow monocytes ( $M_R$ ) recruited at a homeostatic rate  $M_{prod}^*$ . In the presence of GM-CSF, this rate  
 455 increases towards  $\psi_M^{max}$ . Monocytes are also recruited by the presence of infected cells at a maximal  
 456 rate of  $p_{M,I}$  with half-effect  $\epsilon_{I,M}$ , and subsequently disappear through differentiation into inflammatory  
 457 macrophages (as above) or death at rate  $d_M$ .

458 CD8<sup>+</sup> T cells are recruited through antigen presentation on infected cells as a function of  
 459 infected cell numbers at rate  $p_{T,I}$ . The constant delay ( $\tau_T$ ) accounts for the time taken for dendritic cells  
 460 to activate, migrate to the lymph nodes, activate CD8<sup>+</sup> T cells, and the arrival of effector CD8<sup>+</sup> T cells  
 461 at the infection site. CD8<sup>+</sup> T cell expansion occurs in response to bound IFN at a maximal rate  $p_{T,F}$   
 462 with half-effect  $\epsilon_{F,T}$ , and CD8<sup>+</sup> T-cell exhaustion occurs with high concentrations of IL-6 [16, 17], with  
 463 half-effect  $\epsilon_{L,T}$ , and apoptosis occurs at rate  $d_T$ . All variable and parameter descriptions are provided in  
 464 **Table S1**.

#### 465 **Estimating early infection dynamics ('viral model')**

466 To begin estimating parameter values from data, we set all immune populations and cytokine  
 467 concentrations in the full model (Supplementary Information **Eqs. S1-S22**) to zero ( $M_{\Phi R} = M_{\Phi I} =$   
 468  $M = N = T = L_U = L_B = G_U = G_B = C_U = C_B = F_U = F_B = 0$ ). This gives

$$\frac{dV}{dt} = pI - d_V V, \quad 6$$

$$\frac{dS}{dt} = \lambda_S \left( 1 - \frac{S + I + D}{S_{max}} \right) S - \beta SV, \quad 7$$

$$\frac{dI}{dt} = \frac{\beta S(t - \tau_I)V(t - \tau_I)\epsilon_{F,I}}{\epsilon_{F,I} + F_B} - d_I I, \quad 8$$

$$\frac{dD}{dt} = d_I I - d_D D. \quad 9$$

469 We also assumed there were no resistant cells ( $R = 0$ ) due to the absence of an IFN equation. This  
 470 resulted in a simplified ‘viral model’ that considers only virus ( $V$ ) infection of susceptible cells ( $S$ )  
 471 which creates infected cells ( $I$ ) after  $\tau_I$  days, which die through lysis, creating dead cells ( $D$ ).

472 **Type I interferon dynamics during early infection (‘IFN model’)**

473 To study infection dynamics driven uniquely by IFN, we extended **Eqs. 6-9** by introducing the  
 474 IFN mechanisms from **Eqs. S1-S22**, i.e. setting other cytokine and immune cell populations to zero  
 475 ( $M_{\Phi R} = M_{\Phi I} = M = N = T = L_U = L_B = G_U = G_B = C_U = C_B = 0$ ), giving

$$\frac{dV}{dt} = pI - d_V V, \quad 10$$

$$\frac{dS}{dt} = \lambda_S \left(1 - \frac{S + I + R + D}{S_{max}}\right)S - \beta SV, \quad 11$$

$$\frac{dI}{dt} = \frac{\beta S(t - \tau_I)V(t - \tau_I)\epsilon_{F,I}}{\epsilon_{F,I} + F_B} - d_I I, \quad 12$$

$$\frac{dR}{dt} = \lambda_S \left(1 - \frac{S + I + R + D}{S_{max}}\right)R + \frac{\beta SV F_B}{F_B + \epsilon_{F,I}}, \quad 13$$

$$\frac{dD}{dt} = d_I I - d_D D, \quad 14$$

$$\frac{dF_U}{dt} = \psi_F^{prod} + \frac{p_{F,I}I}{I + \eta_{F,I}} - k_{lin_F}F_U - k_{B_F}((T^* + I)A_F - F_B)F_U + k_{U_F}F_B, \quad 15$$

$$\frac{dF_B}{dt} = -k_{int_F}F_B + k_{B_F}((T^* + I)A_F - F_B)F_U - k_{U_F}F_B, \quad 16$$

476 where cells become resistant ( $R$ ) through IFN ( $F_U$  and  $F_B$ ). The parameter  $\psi_F^{prod}$  was introduced to  
 477 account for the production of IFN by macrophages and monocytes not explicitly modelled in this  
 478 reduced system but included in the full system (i.e.  $p_{F,M}$  and  $p_{F,M\Phi}$  in **Eq. S17**). Previously-fit  
 479 parameters were then fixed to their estimated values (**Table S1**) and the value of  $\psi_F^{prod}$  was determined  
 480 by solving  $dF_U/dt = 0$  at homeostasis (i.e.  $V = I = 0$ ), giving  $\psi_F^{prod} = 0.25$ .

481 **Model calibration and parameter estimation**

482 Model parameters (**Table S1**) were obtained either directly from the literature, through fitting  
 483 effect curves (**Eqs. S24-S25**) or sub-models (**Eqs. S26-S56**) to *in vitro* or *in vivo* data, or by calculating

484 the value that ensured that homeostasis was maintained (**Eqs. S57-S70**) in the absence of infection. All  
485 fitting procedures were performed using MATLAB 2019b functions *fmincon* or *lsqnonlin* [71].

486 Initial concentrations of all unbound cytokines ( $L_{U,0}$ ,  $G_{U,0}$ ,  $C_{U,0}$  and  $F_{U,0}$ ), susceptible cells,  
487 resident macrophages, monocytes, neutrophils, and CD8<sup>+</sup> T cells ( $S_0$ ,  $M_{\Phi R,0}$ ,  $M_0$ ,  $N_0$  and  $T_0$ ) were  
488 estimated from plasma and lung tissue concentrations in humans. Parameters for cytokine binding and  
489 unbinding kinetics (**Eqs. 2-4**), such as the molecular weight ( $MM$ ), binding sites per cell ( $K$ ),  
490 binding/unbinding rates ( $k_B$  and  $k_U$ ), internalization rates for GM-CSF, G-CSF and IFN ( $k_{int}$ ), and  
491 cytokine clearance rates ( $k_{lin}$ ), were estimated both from experimental measurements and previous  
492 modelling work. The stoichiometric constants  $POW$  and  $\hat{p}$  were both equal to 1 for all cytokines,  
493 except for G-CSF for which  $POW = 1.4608$  and  $\hat{p} = 2$  as previously estimated by Craig et al. [66].  
494 Neutrophil and monocyte reservoir dynamics, monocyte differentiation, macrophage activation, and  
495 CD8<sup>+</sup> T cell recruitment and expansion parameters were primarily estimated from previous  
496 mathematical modelling studies. Immune cell death rates were taken directly from the literature or  
497 estimated from recorded half-lives using **Eq. S23**.

498 The rates of virus production, decay, infectivity, and infected cell lysis ( $p$ ,  $d_V$ ,  $\beta$  and  $d_I$   
499 respectively) were then estimated by fitting **Eqs. 6-9** to viral load measurements from SARS-CoV-2  
500 infection in macaques [41] where eight adult rhesus macaques inoculated with  $4 \times 10^5$  TCID<sub>50</sub>/ml  
501 ( $3 \times 10^8$  genome copies/ml) SARS-CoV-2 [41] (**Table S1**). Viral loads below 1 copy/ml were  
502 assumed to be negligible. Estimated parameters for viral decay and cell lysis ( $d_V$  and  $d_I$ ) were used as  
503 an upper bound for parameter values in the full model.

504 A subset of parameters was obtained through fitting sigmoidal effect curves (**Eqs. S24-S25**)  
505 curves to *in vitro* and *in vivo* experiments. These include the half-effect neutrophil concentration for  
506 epithelial cell damage, the half-effect concentrations for monocyte production and differentiation  
507 through GM-CSF signalling ( $\epsilon_{G,M}$  and  $\epsilon_{G,M\Phi_I}$ ; **Figure S1**). Other parameters obtained through effect  
508 curves were the half-effects for IL-6 production by monocytes ( $\eta_{L,M}$ ), the effect of IL-6 on monocyte  
509 differentiation ( $\epsilon_{L,M}$ ) and the half-effect of IFN on CD8<sup>+</sup> T cell ( $\epsilon_{F,T}$ ) and IL-6 on CD8<sup>+</sup> T cell  
510 expansion ( $\epsilon_{L,T}$ ) (**Figure S2**).

511 These parameters were then fixed, and remaining parameters were estimated by fitting time-  
512 dependent sub-models of **Eqs. S1-S22** to relevant data. The proliferation rate of epithelial cells ( $\lambda_S$ ), the  
513 internalization rate of IL-6 ( $k_{int_L}$ ), and the rate of neutrophil induced damage were fit to corresponding  
514 time-series measurements using exponential rate terms (**Figure S2**). Clearance and phagocytosis of  
515 infected cells and extracellular virus by inflammatory macrophages ( $\delta_{I,M\Phi}$  and  $\delta_{V,M\Phi}$ ) were fit to *in*

516 *vitro* experiments (**Figure S2**). Production of IFN by macrophages ( $p_{F,M\Phi}$ ) was obtained by fitting to  
517 data measuring IFN- $\alpha$  production (**Figure S3**). The parameters regulating the rate of the resident  
518 macrophage pool replenishment ( $\lambda_{M\Phi}$  and  $\epsilon_{V,M\Phi}$ ) were estimated from *in vivo* observations of resident  
519 macrophages during influenza virus infection (**Figure S3**). GM-CSF production by monocytes  
520 ( $p_{G,M}$ ; **Figure S3**), IFN production by infected cells ( $p_{F,I}$ ), and IL-6 production by infected cells and  
521 macrophages ( $p_{L,I}$  and  $p_{L,M\Phi}$ ) were all obtained from fitting reduced versions of **Eqs. S1-S22** to *in vitro*  
522 experiments [47, 48, 72, 73] (**Figure S4**).

523 Lastly, any remaining parameters values were obtained by ensuring that homeostasis was  
524 maintained in absence of infection (**Figure S5**). Parameters calculated from homeostasis include the  
525 half-effect monocyte concentration for G-CSF production ( $\eta_{C,M}$ ), the production rate of IL-6 and GM-  
526 CSF by inflammatory macrophages ( $p_{L,M\Phi}$  and  $p_{G,M\Phi}$ ), the production rate of monocytes by GM-CSF  
527 ( $p_{M,G}$ ), and the half-effect inflammatory macrophage concentration for IFN production ( $\eta_{F,M\Phi}$ ). For  
528 some parameters it was not possible to obtain an estimation from the literature, and for these we either  
529 set their value equal to an already estimated parameter ( $\epsilon_{L,N}, p_{C,M}, p_{F,M\Phi_I}, \eta_{G,M\Phi}$ ), or qualitatively  
530 estimated it ( $\epsilon_{I,M}, \rho$ ).

531 For the ‘IFN model’ (**Eqs. 10-16**), parameters related to virus ( $p, d_V, \beta$  and  $d_I$ ), epithelial cell  
532 proliferation ( $\lambda_S$  and  $S_{max}$ ), and IFN ( $p_{F,I}, \eta_{F,I}, k_{lin_F}, k_{B_F}, A_F, k_{U_F}$  and  $\epsilon_{F,I}$ ) were fixed to those in **Table**  
533 **S1**.

### 534 Numerical simulations

535 All ODE models were solved using *ode45* in MATLAB, and delay differentiation equations  
536 (i.e. **Eqs. S1-S22**) were solved using *ddesd* in MATLAB.

### 537 Sensitivity analysis

538 We performed a local sensitivity analysis for the full model (**Eqs. S1-S22**) by individually  
539 varying each parameter by  $\pm 20\%$  from its estimated value and quantifying the effect on the model’s  
540 output. This change was recorded and used to evaluate different metrics representing the inflammatory  
541 response to SARS-CoV-2, namely maximum viral load, maximum number of dead cells, minimum  
542 uninfected tissue, maximum number of inflammatory macrophages, maximum number of CD8<sup>+</sup> T cells,  
543 maximum unbound IL-6, maximum unbound IFN, the total exposure (AUC) to type I IFN, number of  
544 days the percent of damaged tissue was  $>80\%$ , and time of unbound type I IFN peak. We quantified the  
545 fraction of undamaged tissue by  $(S + R)/S_{max}$ .

### 546 Virtual patient generation

547 To generate a cohort of 200 virtual patients, we followed techniques similar to those of Allen et  
 548 al. [26] and our previous studies [74, 75] wherein individual virtual patients were created by sampling a  
 549 parameter set  $\mathbf{p}$  from parameter distributions then simulating the model to verify that each individual's  
 550 trajectory was realistic. A subset of parameters ( $p_{M\Phi_I,L}$ ,  $p_{L,M\Phi}$ ,  $p_{F,I}$ ,  $p_{M,I}$ ,  $\eta_{F,M\Phi}$ ,  $\epsilon_{F,I}$ , and  $p_{F,M}$ ) was  
 551 designated as patient-specific after considering the results of the sensitivity analysis and standard  
 552 deviations inferred from clinical observations (Supplementary Information). To avoid the inclusion of  
 553 unrealistic dynamics, patient parameter sets were then optimized using simulated annealing to ensure  
 554 predictions fell within physiological ranges for viral load [41], IL-6 [6, 44], IFN- $\alpha$  [42], and G-CSF  
 555 [24] (**Figure 7**).

556 The upper  $u_i$  and lower  $l_i$  bounds for  $V$ ,  $L_U$ ,  $F_U$  and  $C_U$  were based off these physiological  
 557 ranges from Munster et al. [41] (viral loads), Herold et al. [44] (IL-6 concentrations), Trouillet-Assant  
 558 et al. [42] (IFN dynamics), and Liu et al. [7] (G-CSF concentrations) as described in Supplementary  
 559 Information Section S.6.1. Intervals for each patient-specific parameter set were restricted to four  
 560 standard deviations from the mean or zero if the lower bound was negative. Given an initial patient  
 561 specific parameter set  $\mathbf{p}$ , we used simulated annealing to minimize  $J(\mathbf{p})$ , i.e.

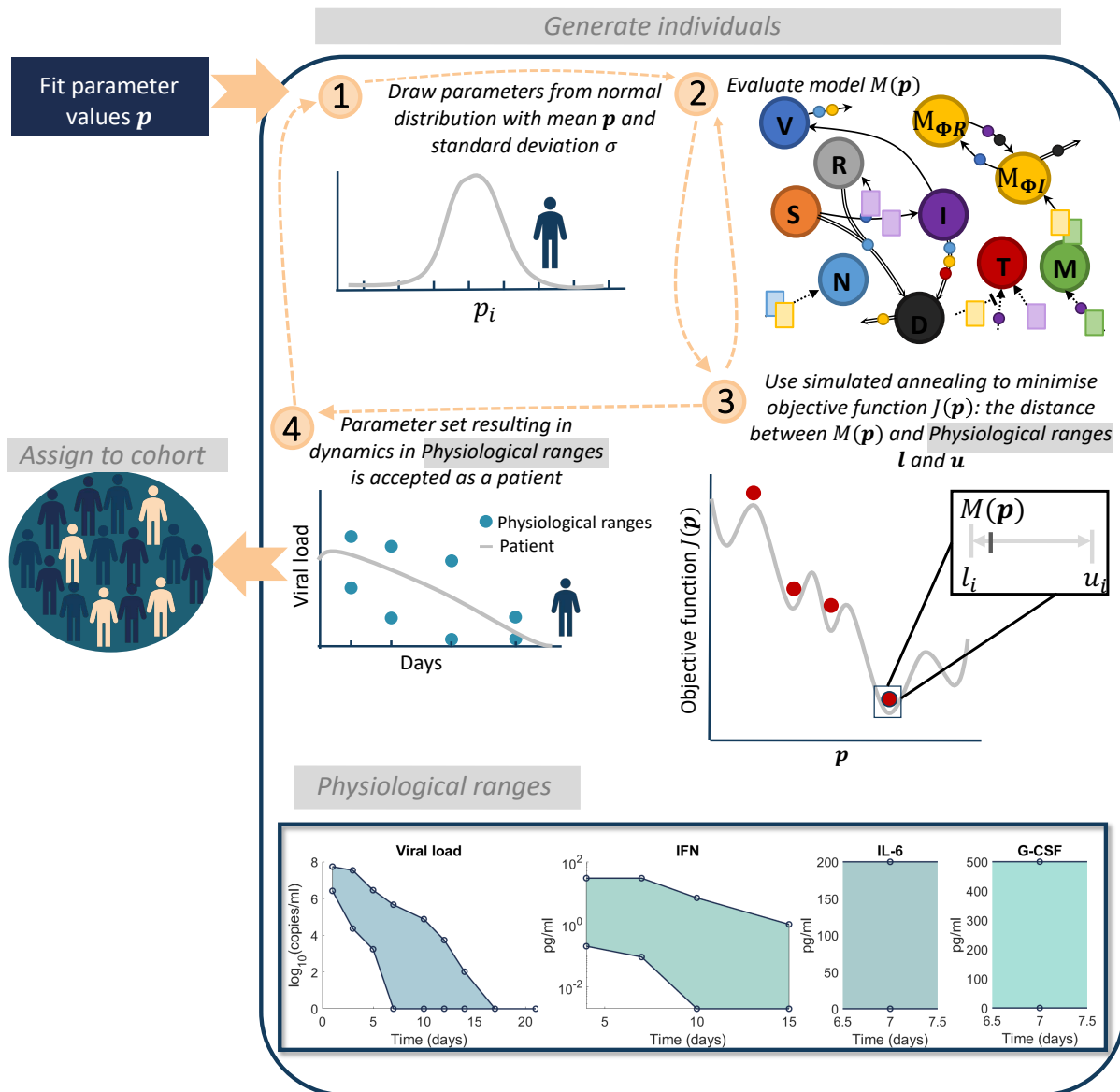
$$\min_{\mathbf{p}} J(\mathbf{p}) = \min_{\mathbf{p}} \left[ \sum_i \max \left( \left( M_i(\mathbf{p}) - \frac{l_i + u_i}{2} \right)^2 - \left( u_i - \frac{l_i + u_i}{2} \right)^2, 0 \right) \right], \quad 17$$

562 where  $M_i(\mathbf{p})$  is the model output  $i$  evaluated at parameter set  $\mathbf{p}$  corresponding to the upper and lower  
 563 bound  $l_i$  and  $u_i$  (**Figure 7**).

564 To quantify disease severity for each patient, we introduced an inflammation variable ( $\Psi$ ) to  
 565 account for the combined changes in IL-6 ( $L_U$ ), neutrophils ( $N$ ), and damaged tissue ( $S + R$ ), each  
 566 normalized by the virtual cohort's average. In this way,  $\Psi$  measures an individual's relative change  
 567 from the cohort's baseline, and quantifies the contributions of IL-6, neutrophils, and tissue damage on  
 568 comparable scales. For a given patient  $j$ , the inflammation marker is given by

$$\begin{aligned} \Psi^j = & \frac{\max_t(L_U^j(t))}{\frac{1}{n} \sum_{j=1}^n (\max_t(L_U^j(t)))} + \frac{\max_t(N^j(t))}{\frac{1}{n} \sum_{j=1}^n (\max_t(N^j(t)))} \\ & + \frac{S_{max} - \min_t(S^j(t) + R^j(t))}{\frac{1}{n} \sum_{j=1}^n (S_{max} - \min_t(S^j(t) + R^j(t)))}, \end{aligned} \quad 18$$

569 where  $n$  is the total number of patients in the cohort, and  $L_U^j$ ,  $N^j$ ,  $S^j$ , and  $R^j$  are the unbound IL-6,  
 570 neutrophils, and susceptible and resistant epithelial cell count, respectively.



571

572 **Figure 7. Algorithm for generating virtual patients.** Parameters in the model were first obtained through  
 573 fitting to data (Table S1). 1) Parameters relating to macrophage, IL-6 and IFN production  
 574 ( $p_{M\Phi,I}$ ,  $p_{L,M\Phi}$ ,  $p_{F,I}$ ,  $p_{M,I}$ ,  $\eta_{F,M\Phi}$ ,  $\epsilon_{F,I}$ , and  $p_{F,M}$ ) were generated from normal distributions with mean equal to  
 575 their original fitted values and standard deviation informed by experiment observations (see Section S6.1). 2) The model evaluated is then evaluated on this parameter set to obtain  $y(t, p)$ . 3) A simulated annealing  
 576 algorithm is then used to determine a parameter set that optimises the objective function  $J(p)$  (Eq.16). 4)  
 577 Optimizing the objective function provides a parameter set for which the patient response to SARS-CoV-2 will  
 578 be within the physiological ranges. This patient is then assigned to the cohort and this process is continued until  
 579 200 patients have been generated. Physiological ranges are noted in the bottom box for viral load [41], IFN [42],  
 580 IL-6 [44] and G-CSF [7].

582 **Statistical analyses**

583 The Pearson correlation coefficient (R) was used to measure the degree of interaction between two  
 584 variables, with a significance level of  $\alpha < 0.05$  indicating rejection of the hypothesis that there is no  
 585 relationship between the observed variables. In addition, we used two-sample two-sided t-tests (number

586 of patients  $< 40$ ) and z-tests (number of patients  $\geq 40$ ) at the  $\alpha < 0.05$  significance level to test the  
587 hypothesis that there were no differences between sample means.

## 588 **Acknowledgments**

589 All authors would like to thank Paul Macklin and Thomas Hillen for encouraging collaboration.

## 590 **Funding**

591 ALJ was supported by Fonds de recherche Santé Québec Programme de bourse de formation  
592 postdoctorale pour les citoyens d'autres pays and a Centre for Applied Mathematics in Bioscience and  
593 Medicine (CAMBAM) Postdoctoral fellowship. RA and AMS were supported by NIH R01 AI139088.  
594 ALJ and MC were supported by NSERC Discovery Grant RGPIN-2018-04546 and NSERC Alliance  
595 COVID-19 ALLRP 554923 – 20.

## 596 **Author contributions**

597 ALJ, RA, AMS, CLD, and MC conceived the study. AMS and APS conducted the alveolar  
598 macrophage and viral load *in vivo* experiments. PAM contributed significant immunological insight.  
599 All authors contributed intellectual insight into the development of the study. ALJ and MC wrote the  
600 code and manuscript with significant contributions from all authors.

## 601 **Competing interests**

602 The authors declare no competing interests.

## 603 **Data and materials availability**

604 All data needed to evaluate the conclusions in the paper are present in the paper and/or the  
605 Supplementary Materials.”). Sample code is available upon reasonable request to the corresponding  
606 author.

## 607 **References**

- 608 1. Mehta P, McAuley DF, Brown M, Sanchez E, Tattersall RS, Manson JJ. COVID-19: consider  
609 cytokine storm syndromes and immunosuppression. *Lancet*. 2020;395(10229):1033-1034.  
610 doi:[https://doi.org/10.1016/S0140-6736\(20\)30628-0](https://doi.org/10.1016/S0140-6736(20)30628-0)
- 611 2. Zhou P, Yang X-L, Wang X-G, et al. A pneumonia outbreak associated with a new coronavirus  
612 of probable bat origin. *Nature*. 2020;579(7798):270-273. doi:10.1038/s41586-020-2012-7
- 613 3. Qin C, Zhou L, Hu Z, et al. Dysregulation of immune response in patients with COVID-19 in  
614 Wuhan, China. *Prepr with Lancet*. 2020;February 1:1-18.
- 615 4. Wu F, Zhao S, Yu B, et al. A new coronavirus associated with human respiratory disease in  
616 China. *Nature*. 2020;579(7798):265-269. doi:10.1038/s41586-020-2008-3
- 617 5. Stebbing J, Phelan A, Griffin I, et al. COVID-19: combining antiviral and anti-inflammatory  
618 treatments. *Lancet Infect Dis*. 2020;20(4):400-402. doi:[https://doi.org/10.1016/S1473-3099\(20\)30132-8](https://doi.org/10.1016/S1473-3099(20)30132-8)
- 619 6. Lucas C, Wong P, Klein J, et al. Longitudinal analyses reveal immunological misfiring in severe  
620 COVID-19. *Nature*. 2020;1-9.
- 621 7. Liu J, Li S, Liu J, et al. Longitudinal characteristics of lymphocyte responses and cytokine  
622 profiles in the peripheral blood of SARS-CoV-2 infected patients. *EBioMedicine*. 2020;102763.
- 623 8. Duployez N, Demonchy J, Berthon C, et al. Clinico-biological features and clonal hematopoiesis  
624 in patients with severe covid-19. *Cancers (Basel)*. 2020;12(7):1-11.  
625 doi:10.3390/cancers12071992
- 626 9. Nathan C. Neutrophils and COVID-19: Nots, NETs, and knots. *J Exp Med*.  
627 2020;217(9):e20201439.
- 628 10. Jamilloux Y, Henry T, Belot A, et al. Should we stimulate or suppress immune responses in

630        COVID-19? Cytokine and anti-cytokine interventions. *Autoimmun Rev.* 2020;102567.  
631        doi:10.1016/j.autrev.2020.102567

632        11. Mathew D, Giles JR, Baxter AE, et al. Deep immune profiling of COVID-19 patients reveals  
633        distinct immunotypes with therapeutic implications. *Science (80- ).*  
634        2020;1209(September):eabc8511. doi:10.1126/science.abc8511

635        12. Blanco-Melo D, Nilsson-Payant BE, Liu W-C, et al. Imbalanced host response to SARS-CoV-2  
636        drives development of COVID-19. *Cell.* 2020;181(5):1036-1045.e9.

637        13. Channappanavar R, Fehr AR, Zheng J, et al. IFN-I response timing relative to virus replication  
638        determines MERS coronavirus infection outcomes. *J Clin Invest.* 2019;129(9):3625-3639.  
639        doi:10.1172/JCI126363

640        14. Channappanavar R, Fehr AR, Vijay R, et al. Dysregulated type I interferon and inflammatory  
641        monocyte-macrophage responses cause lethal pneumonia in SARS-CoV-infected mice. *Cell*  
642        *Host Microbe.* 2016;19(2):181-193. doi:<https://doi.org/10.1016/j.chom.2016.01.007>

643        15. Li B, Jones LL, Geiger TL. IL-6 promotes T cell proliferation and expansion under  
644        inflammatory conditions in association with low-level ROR $\gamma$ t expression. *J Immunol.*  
645        2018;201(10):2934-2946.

646        16. Liu T, Zhang J, Yang Y, et al. The role of interleukin-6 in monitoring severe case of coronavirus  
647        disease 2019. *EMBO Mol Med.* 2020.

648        17. Laing AG, Lorenc A, del Molino del Barrio I, et al. A dynamic COVID-19 immune signature  
649        includes associations with poor prognosis. *Nat Med.* 2020. doi:10.1038/s41591-020-1038-6

650        18. Bastard P, Rosen LB, Zhang Q, et al. Auto-antibodies against type I IFNs in patients with life-  
651        threatening COVID-19. *Science (80- ).* 2020;4585:eabd4585. doi:10.1126/science.abd4585

652        19. Seo Y-J, Hahn B. Type I interferon modulates the battle of host immune system against viruses.  
653        *Adv Appl Microbiol.* 2010;73:83-101. doi:10.1016/S0065-2164(10)73004-5

654        20. Arnaud P. The interferons: pharmacology, mechanism of action, tolerance and side effects. *La*  
655        *Rev Med interne.* 2002;23:449s-458s.

656        21. Smith AM, Perelson AS. Influenza A virus infection kinetics: quantitative data and models.  
657        *Wiley Interdiscip Rev Syst Biol Med.* 2011;3(4):429-445. doi:10.1002/wsbm.129

658        22. Jamilloux Y, Henry T, Belot A, et al. Should we stimulate or suppress immune responses in  
659        COVID-19? Cytokine and anti-cytokine interventions. *Autoimmun Rev.* 2020.

660        23. Widagdo W, Okba NMA, Stalin Raj V, Haagmans BL. MERS-coronavirus: From discovery to  
661        intervention. *One Heal.* 2017;3:11-16. doi:<https://doi.org/10.1016/j.onehlt.2016.12.001>

662        24. Long Q-X, Tang X-J, Shi Q-L, et al. Clinical and immunological assessment of asymptomatic  
663        SARS-CoV-2 infections. *Nat Med.* 2020;1-5.

664        25. Jenner AL, Aogo RA, Davis CL, Smith AM, Craig M. Leveraging Computational Modelling to  
665        Understand Infectious Diseases. *Curr Pathobiol Rep.* 2020;In press.

666        26. Allen RJ, Rieger TR, Musante CJ. Efficient Generation and Selection of Virtual Populations in  
667        Quantitative Systems Pharmacology Models. *CPT Pharmacometrics Syst Pharmacol.*  
668        2016;5(3):140-146. doi:10.1002/psp4.12063

669        27. Cassidy T, Humphries AR, Craig M, Mackey MC. Characterizing chemotherapy-induced  
670        neutropenia and monocytopenia through mathematical modelling. *bioRxiv.*  
671        2020:2020.04.02.022046. doi:10.1101/2020.04.02.022046

672        28. Alfonso S, Jenner AL, Craig M. Translational approaches to treating dynamical diseases through  
673        in silico clinical trials. *Chaos An Interdiscip J Nonlinear Sci.* 2020;In review.

674        29. Smith AM. Host-pathogen kinetics during influenza infection and coinfection: insights from  
675        predictive modeling. *Immunol Rev.* 2018;285(1):97-112.

676        30. Jenner AL, Yun C-O, Yoon A, Coster ACF, Kim PS. Modelling combined virotherapy and  
677        immunotherapy: strengthening the antitumour immune response mediated by IL-12 and GM-  
678        CSF expression. *Lett Biomath.* 2018;5(sup1). doi:10.1080/23737867.2018.1438216

679 31. Goyal A, Cardozo-Ojeda EF, Schiffer JT. Potency and timing of antiviral therapy as  
680 determinants of duration of SARS CoV-2 shedding and intensity of inflammatory response.  
681 *medRxiv*. 2020:2020.04.10.20061325. doi:10.1101/2020.04.10.20061325

682 32. Waghmare A, Krantz EM, Baral S, et al. Reliability of self-sampling for accurate assessment of  
683 respiratory virus viral and immunologic kinetics. *medRxiv*. January 2020:2020.04.03.20051706.  
684 doi:10.1101/2020.04.03.20051706

685 33. Kim KS, Ejima K, Ito Y, et al. Modelling SARS-CoV-2 dynamics: implications for therapy.  
686 *medRxiv*. January 2020:2020.03.23.20040493. doi:10.1101/2020.03.23.20040493

687 34. Ejima K, Kim KS, Ito Y, et al. Inferring timing of infection using within-host SARS-CoV-2  
688 infection dynamics model: Are “imported cases” truly imported? *medRxiv*. January  
689 2020:2020.03.30.20040519. doi:10.1101/2020.03.30.20040519

690 35. Sahoo S, Hari K, Jhunjhunwala S, Jolly MK. Mechanistic modeling of the SARS-CoV-2 and  
691 immune system interplay unravels design principles for diverse clinicopathological outcomes.  
692 *bioRxiv*. January 2020:2020.05.16.097238. doi:10.1101/2020.05.16.097238

693 36. Sego T, Aponte-Serrano JO, Gianlupi JF, et al. A modular framework for multiscale  
694 multicellular spatial modeling of viral infection, immune response and drug therapy timing and  
695 efficacy in epithelial tissues: A multiscale model of viral infection in epithelial tissues. *BioRxiv*.  
696 2020.

697 37. Sadler AJ, Williams BRG. Interferon-inducible antiviral effectors. *Nat Rev Immunol*.  
698 2008;8(7):559-568.

699 38. Chomarat P, Banchereau J, Davoust J, Karolina Palucka A. IL-6 switches the differentiation of  
700 monocytes from dendritic cells to macrophages. *Nat Immunol*. 2000;1(6):510-514.  
701 doi:10.1038/82763

702 39. Drescher, Brandon and Bai F. Neutrophil in viral infections, friend or foe? *Virus Res*.  
703 2013;171(1):1-7.

704 40. Galani IE, Andreakos E. Neutrophils in viral infections: current concepts and caveats. *J Leukoc  
705 Biol*. 2015;98(4):557-564. doi:10.1189/jlb.4VMR1114-555R

706 41. Munster VJ, Feldmann F, Williamson BN, et al. Respiratory disease in rhesus macaques  
707 inoculated with SARS-CoV-2. *Nature*. 2020. doi:10.1038/s41586-020-2324-7

708 42. Trouillet-Assant S, Viel S, Gaymard A, et al. Type I IFN immunoprofiling in COVID-19  
709 patients. *J Allergy Clin Immunol*. 2020:4-8. doi:10.1016/j.jaci.2020.04.029

710 43. Zhao Y, Qin L, Zhang P, et al. Longitudinal COVID-19 profiling associates IL-1Ra and IL-10  
711 with disease severity and RANTES with mild disease. *JCI Insight*. 2020;5(13).  
712 doi:10.1172/jci.insight.139834

713 44. Herold T, Jurinovic V, Arnreich C, et al. Elevated levels of interleukin-6 and CRP predict the  
714 need for mechanical ventilation in COVID-19. *J Allergy Clin Immunol*. 2020.

715 45. Sheahan TP, Sims AC, Leist SR, et al. Comparative therapeutic efficacy of remdesivir and  
716 combination lopinavir, ritonavir, and interferon beta against MERS-CoV. *Nat Commun*.  
717 2020;11(1):222. doi:10.1038/s41467-019-13940-6

718 46. Kratofil RM, Kubes P, Deniset JF. Monocyte conversion during inflammation and injury.  
719 *Arterioscler Thromb Vasc Biol*. 2017;37(1):35-42.

720 47. Shibata Y, Berclaz P-Y, Chroneos ZC, Yoshida M, Whitsett JA, Trapnell BC. GM-CSF  
721 Regulates Alveolar Macrophage Differentiation and Innate Immunity in the Lung through PU.1.  
722 *Immunity*. 2001;15(4):557-567. doi:10.1016/S1074-7613(01)00218-7

723 48. Ioannidis I, Ye F, McNally B, Willette M, Flaño E. Toll-Like Receptor Expression and  
724 Induction of Type I and Type III Interferons in Primary Airway Epithelial Cells. *J Virol*.  
725 2013;87(6):3261. doi:10.1128/JVI.01956-12

726 49. Pawelek KA, Dor Jr D, Salmeron C, Handel A. Within-host models of high and low pathogenic  
727 influenza virus infections: The role of macrophages. *PLoS One*. 2016;11(2):2016.

728 50. Eftimie R, Eftimie G. Tumour-associated macrophages and oncolytic virotherapies: a  
729 mathematical investigation into a complex dynamics. *Lett Biomath.* 2018;5(sup1):S6-S35.  
730 doi:10.1080/23737867.2018.1430518

731 51. Patel AA, Zhang Y, Fullerton JN, et al. The fate and lifespan of human monocyte subsets in  
732 steady state and systemic inflammation. *J Exp Med.* 2017;214(7):1913-1923.

733 52. Krummel MF, Mahale JN, Uhl LF, et al. Paracrine costimulation of IFN-\$\gamma\$ signaling by  
734 integrins modulates CD8 T cell differentiation. *Proc Natl Acad Sci.* 2018;115(45):11585-11590.

735 53. Ohta M, Okabe T, Ozawa K, Urabe A, Takaku F. 1,25-Dihydroxy vitamin D<sub>3</sub> (calcitriol)  
736 stimulates proliferation of human circulating monocytes in vitro. *FEBS Lett.* 1985;185(1):9-13.  
737 doi:10.1016/0014-5793(85)80730-4

738 54. Krilov LR, Hendry RM, Godfrey E, McIntosh K. Respiratory Virus Infection of Peripheral  
739 Blood Monocytes: Correlation with Ageing of Cells and Interferon Production in vitro. *J Gen  
740 Virol.* 1987;68(6):1749-1753. doi:<https://doi.org/10.1099/0022-1317-68-6-1749>

741 55. Goudot C, Coillard A, Villani A-C, et al. Aryl hydrocarbon receptor controls monocyte  
742 differentiation into dendritic cells versus macrophages. *Immunity.* 2017;47(3):582-596.

743 56. Desalegn G, Pabst O. Inflammation triggers immediate rather than progressive changes in  
744 monocyte differentiation in the small intestine. *Nat Commun.* 2019;10(1):1-14.

745 57. Karki R, Raj B, Tuladher, S et al. COVID-19 cytokines and the hyperactive immune response:  
746 Synergism of TNF- $\alpha$  and IFN- $\gamma$  in triggering inflammation, tissue damage, and death. *bioRxiv.*  
747 2020:2020.10.29.361048.

748 58. Della-Torre E, Campochiaro C, Cavalli G, et al. Interleukin-6 blockade with sarilumab in severe  
749 COVID-19 pneumonia with systemic hyperinflammation: an open-label cohort study. *Ann  
750 Rheum Dis.* 2020;79(10):1277-1285.

751 59. Santillán M. On the use of the Hill functions in mathematical models of gene regulatory  
752 networks. *Math Model Nat Phenom.* 2008;3(2):85-97.

753 60. Janeway C. *Immunobiology 5: The Immune System in Health and Disease.* New York: Garland  
754 Pub.; 2001.

755 61. Louten J. Virus Transmission and Epidemiology. In: *Essential Human Virology*. Elsevier;  
756 2016:71-92. doi:10.1016/b978-0-12-800947-5.00005-3

757 62. Nagarajan UM. Induction and function of IFN $\beta$  during viral and bacterial infection. *Crit Rev  
758 Immunol.* 2011;31(6):459-474. doi:10.1615/critrevimmunol.v31.i6.20

759 63. Arnaud P. Different interferons: Pharmacology, pharmacokinetics, proposed mechanisms, safety  
760 and side effects. *Rev Med Interne.* 2002;23(SUPPL. 4):449S-458S. doi:10.1016/S0248-  
761 8663(02)00659-8

762 64. Elmore S. Apoptosis: a review of programmed cell death. *Toxicol Pathol.* 2007;35(4):495-516.  
763 doi:10.1080/01926230701320337

764 65. Klöditz K, Fadeel B. Three cell deaths and a funeral: macrophage clearance of cells undergoing  
765 distinct modes of cell death. *Cell death Discov.* 2019;5(1):1-9.

766 66. Craig M, Humphries AR, Mackey MC. A Mathematical Model of Granulopoiesis Incorporating  
767 the Negative Feedback Dynamics and Kinetics of G-CSF/Neutrophil Binding and  
768 Internalization. *Bull Math Biol.* 2016;78(12):2304-2357. doi:10.1007/s11538-016-0179-8

769 67. Shi Y, Liu CH, Roberts AI, et al. Granulocyte-macrophage colony-stimulating factor (GM-CSF)  
770 and T-cell responses: what we do and don't know. *Cell Res.* 2006;16(2):126-133.

771 68. Takei Y, Ando H, Tsutsui K, eds. About the Editors. In: *Handbook of Hormones.* San Diego:  
772 Academic Press; 2016:v. doi:<https://doi.org/10.1016/B978-0-12-801028-0.00292-0>

773 69. Scheller J, Chalaris A, Schmidt-Arras D, Rose-John S. The pro-and anti-inflammatory properties  
774 of the cytokine interleukin-6. *Biochim Biophys Acta (BBA)-Molecular Cell Res.*  
775 2011;1813(5):878-888.

776 70. Rösler B, Herold S. Lung epithelial GM-CSF improves host defense function and epithelial

777 repair in influenza virus pneumonia—a new therapeutic strategy? *Mol Cell Pediatr.*  
778 2016;3(1):29. doi:10.1186/s40348-016-0055-5

779 71. Matlab 2019a. 2019.

780 72. Lee M-T, Kaushansky K, Ralph P, Ladner MB. Differential Expression of M-CSF, G-CSF, and  
781 GM-CSF by Human Monocytes. *J Leukoc Biol.* 1990;47(3):275-282. doi:10.1002/jlb.47.3.275

782 73. Ye S, Lowther S, Stambas J. Inhibition of reactive oxygen species production ameliorates  
783 inflammation induced by influenza A viruses via upregulation of SOCS1 and SOCS3. *J Virol.*  
784 2015;89(5):2672-2683.

785 74. Jenner AL, Cassidy T, Belaid K, Bourgeois-Daigneault M-C, Craig M. In silico trials predict  
786 that combination strategies for enhancing vesicular stomatitis oncolytic virus are determined by  
787 tumour aggressivity. *J Immunother Cancer.* 2020;In review.

788 75. Cassidy T, Craig M. Determinants of combination GM-CSF immunotherapy and oncolytic  
789 virotherapy success identified through in silico treatment personalization. Goldman A, ed. *PLOS*  
790 *Comput Biol.* 2019;15(11):e1007495. doi:10.1371/journal.pcbi.1007495

791

## 792 Supporting information captions

793

### 794 Supplementary Information file.

795 **Figure S1. Effects of neutrophils on lung epithelial cells, GM-CSF on monocyte production and**  
796 **differentiation, the relationships between monocytes and CD4+ T cells with IL-6, and the**  
797 **influence of IFN on T cell expansion. A)** Using the measurements by Knaapen et al.<sup>22</sup>, the  
798 inhibitory effect curve E (Eq. S25) was fit to the cell viability of RLE cells under various  
799 concentrations of H<sub>2</sub>O<sub>2</sub>. **B)** The stimulatory effect curve E (Eq. S24) was fit to the dose response  
800 measurements of blood monoculture cells ( $3 \times 10^3$  cells/dish) with various concentrations of  
801 murine recombinant GM-CSF (IU/ml)<sup>18</sup>. **C)** The stimulatory effect curve E (Eq. S24) was fit to  
802 measurements for the monocytic myeloid cell count as a function of GM-CSF.<sup>17</sup> **D)** Eq. S27 fit  
803 to time course data of IL-6 production from monocytes<sup>38</sup>. **E)** IL-6 stimulation of monocyte  
804 differentiation to macrophages modelled by the inhibitory effect curve E (Eq. S24) fit to the  
805 percentage of CD14+ cells (macrophages) as a function of the number of fibroblasts measured  
806 by Chomarat et al.<sup>16</sup>. **F)** Stimulatory effect curve E (Eq. S24) for IFN- $\gamma$  stimulation on CD8+ T  
807 cells fit to measurements of the signalling in CD8+T cells for varying doses of IFN- $\gamma$ <sup>19</sup>. Data  
808 (black) is plotted as either circles (**D & E**) or mean and standard deviation error bars (**A-C&F**);  
809 solid blue line: corresponding fit.

810 **Figure S2. Dynamics of IL-6 on T cell expansion, epithelial cell growth, IL-6 internalization,**  
811 **neutrophil-induced damage, and macrophage phagocytosis. A)** Effect curve (Eq. S24) for  
812 the IL-6 effect on T cell expansion fit to measurements CD4+ T cells from dilutions of IL-6 by  
813 Holsti and Raulet<sup>21</sup>. **B)** Exponential growth curve fit to the growth of A549 cells<sup>2</sup> **C)** The  
814 internalization rate of IL-6 (Eq. S30) fit to the fraction of internalized IL-6<sup>47</sup>. **D)** Exponential  
815 decay fit to cell viability after H<sub>2</sub>O<sub>2</sub> administration<sup>24</sup>. **E)** The macrophage clearance of apoptotic  
816 material (Eqs. S31-S33) was fit to the percentage of macrophages that had engulfed material  
817 over 25 hours<sup>27</sup>. **F)** The phagocytosis rate of extracellular virus by macrophages was obtained by  
818 fitting Eqs. S34-S35 to the uptake of virus by macrophages measured by Rigden et al.<sup>23</sup>. Data  
819 (black) is plotted as either circles (**A & F**) or mean and standard deviation error bars (**B-E**); solid  
820 blue line: corresponding fit.

821 **Figure S3. Monocyte expansion and type I IFN production by monocytes, alveolar macrophage**  
822 **replenishment after viral infection, and GM-CSF production by monocytes. A)** Eq. S37 fit  
823 to time course of proliferation of monocytes in culture<sup>42</sup>. **B)** Fit of Eqs. S38-S39 to the  
824 production of IFN- $\alpha$  by monocytes after 24 hours with RSV as a function of the number of days

825 of pre-culturing (1, 2, 4 or 7)<sup>43</sup>. **C**) Correlation between infectious virus titre and RT-PCR copy  
826 number for influenza A and B measured by Laurie et al.<sup>88</sup> The relative TCID<sub>50</sub> compared to the  
827 RNA copies is plotted for each virus strain and the mean as a black dashed line. **D-E**) Fit of **Eqs.**  
828 **S40-S42** to viral loads<sup>87</sup> and alveolar macrophages from experimental influenza infections. **F**)  
829 The production of GM-CSF from stimulated monocytes was recorded by Lee et al.<sup>40</sup> Using a  
830 simplified version of the full model (**Eqs. S43-S46**), we obtained the production rates for  
831 monocytes and GM-CSF. Data (black) is plotted as either circles/stars (**B&F**) or mean and  
832 standard deviation error bars (**A,D-E**); solid blue line: corresponding fit.

833 **Figure S4. Production of IFN and IL-6 by infected cells and macrophages.** **A)** Concentration of  
834 IFN- $\beta$  released by alveolar epithelial cells in response to stimulation with influenza virus  
835 recorded at 8, 16 and 24 hours<sup>41</sup>. **B-C)** IL-6 production by infected cells in response to **A)** H5NA  
836 and **B)** H7N9, measured by Ye et al.<sup>36</sup> Data (black) is plotted as mean and standard deviation  
837 error bars with the corresponding fit (**Eqs. S51-S54**) in solid blue. **D)** IL-6 production by  
838 macrophages (**Eq. S56**) in response to stimulation with LPS of varying dosage sizes. Shibata et  
839 al.<sup>37</sup> measured the production of IL-6 for different dosages of LPS and fitting the production  
840 rate to this data to obtain  $p_{L,M\Phi}$ ,  $\eta_{L,M\Phi}$ .

841 **Figure S5. Homeostatic disease-free system regulation.** **A)** To confirm that parameters in the model  
842 represented realistic immunocompetent individuals in the disease-free scenario, **Eqs. S1-S22**  
843 were simulated where  $V_0 = 0$  and parameters were given by the homeostasis **Eqs. S57-S70**. The  
844 initial concentration of G-CSF was perturbed and compared to simulations of the model at  
845 homeostasis. Simulations at homeostasis are represented by solid lines (purple) and perturbed  
846 simulations as dashed lines (pink). **B)** The maximum residual between variables and their initial  
847 conditions at day 50 was measured to confirm that the system was stable for perturbations in all  
848 immune cells and cytokines.

849 **Figure S6. Model validation against human cytokine measurements during SARS-CoV-2**  
850 **infection.** **A)** IFN dynamics of the reduced model (**Figure 3 Main Text**) overlaid with patient  
851 IFN- $\alpha$ 2 plasma concentrations from Trouillet-Assant et al.<sup>70</sup> The solid line (purple) represents  
852 the unbound IFN dynamics from the reduced model (**Eqs. 27-33**). Individual patient IFN- $\alpha$ 2  
853 measurements are plotted as grey circles. Normal IFN- $\alpha$ 2 concentration in healthy volunteers  
854 are indicated by a grey area. **B-F)** Mild and severe dynamics (**Eqs. S1-S22**) corresponding to  
855 simulations in **Figure 4 Main Text** and **Figure S7** overlaid with measurements from the  
856 literature with solid lines: mild disease dynamics; dashed lines: severe disease dynamics. **B-C)**  
857 Plasma IFN- $\alpha$  and IL-6 in COVID-19 critically ill patients (n=26) obtained by Trouillet-Assant  
858 et al.<sup>70</sup> overlaid with mild and severe unbound IFN ( $F_U(t)$ ) and mild and severe unbound IL-6  
859 ( $L_U(t)$ ). **D)** IL-6 levels in patients requiring and not requiring mechanical ventilation obtained  
860 by Herold et al.<sup>91</sup> overlaid with mild and severe unbound IL-6 dynamics. **E-F)** IL-6 and G-CSF  
861 plasma concentration obtained by Long et al.<sup>92</sup> in symptomatic “S” and asymptomatic “AS”  
862 COVID-19 patients overlaid with corresponding mild and severe model dynamics.

863 **Figure S7. Predicting mild and severe COVID-19 dynamics (all model variables).** Extension of  
864 results of mild and severe disease dynamics in **Figure 4 Main Text**. Mild disease (solid lines)  
865 dynamics obtained by using baseline parameter estimates (**Tables S1**) while severe disease  
866 dynamics (dashed lines) were obtained by decreasing the production rate of type I IFN,  $p_{F,I}$ , and  
867 increasing the production of monocytes,  $p_{M,I}$ , and their differentiation to macrophages,  $\eta_{F,M\Phi}$ .  
868 **A)** Lung cells concentrations (susceptible cells  $S(t)$ , resistant cells  $R(t)$ , infected cells  $I(t)$ , dead  
869 cells  $D(t)$  and virus  $V(t)$ ). Solid black line with error bars indicates macaque data (see **Fig. 2**  
870 **Main Text**). **B)** Immune cell concentrations (resident macrophages  $M_{\Phi R}(t)$ , inflammatory  
871 macrophages  $M_{\Phi I}(t)$ , monocytes  $M(t)$ , neutrophils  $N(t)$  and T cells  $T(t)$ ). **C)** Bound and  
872 unbound cytokine concentrations (IL-6 unbound  $L_U(t)$  and bound  $L_B(t)$ , GM-CSF unbound

873  $G_U(t)$  and bound  $G_B(t)$ , G-CSF unbound  $C_U(t)$  and bound  $C_B(t)$ , type I IFN unbound  $F_U(t)$  and  
874 bound  $F_B(t)$ .

875 **Figure S8. Full analysis of parameters driving COVID-19 severity.** A local sensitivity analysis was  
876 performed by varying each parameter  $\pm 20\%$  from its originally estimated value and simulating  
877 the model. Predictions were then compared to baseline considering: Maximum viral load  
878 ( $\max(V)$ ), maximum concentration of dead cells ( $\max(D)$ ), minimum uninfected live cells  
879 ( $\min(S+R)$ ), maximum concentration of inflammatory macrophages ( $\max(M_{\phi_I})$ ), maximum  
880 number of CD8<sup>+</sup> T cells ( $\max(T)$ ), maximum concentration of IL-6 ( $\max(L_U)$ ), maximum  
881 concentration of type I IFN ( $\max(F_U)$ ), the total exposure to type I IFN ( $F_U$  exposure), the  
882 number of days damaged tissue was  $>80\%$  (time  $(S + R)/S_{max} < 0.2$ ), and the day type I IFN  
883 reached its maximum (day  $\max(F_U)$ ). The heatmaps show the fold change of each metric, where  
884 blue signifies the minimum value observed and red signifies the maximum value observed, or by  
885 the number of days, where light to dark pink signifying increasing number of days from zero.  
886 The most sensitive parameters are shown in **Figure 5 in the Main Text**.

887 **Figure S9. Cohort dynamics within physiological ranges.** Virtual patients were generated so that  
888 viral load, IFN and IL-6 concentration were within physiological ranges obtained in the  
889 literature. The physiological ranges (denoted by open circles) were obtained from **A**) Munster et  
890 al.<sup>96</sup>, **B**) Trouillet-Assant et al.<sup>70</sup>, and **C**) Herold et al.<sup>91</sup>. Patient dynamics at discrete time points  
891 are plotted as joined green dots.

892 **Table S1. Parameter values used in the Main Text.** Parameters have been grouped into: (a-e) cell  
893 related, (f-k) cytokine related parameters (l) and initial conditions. Relevant references are given  
894 estimated parameters. Parameters obtained through fitting to data in the literature have the  
895 appropriate figure noted in the Info column. Parameters estimated from homeostasis calculation  
896 are denoted by H or qualitatively estimated by E. Parameters whose value was taken from  
897 another parameters estimated has that parameter noted. Viral load is reported as virion copies  
898 and cells have been noted in  $10^9$  cells. Time t is in days. The final sub-table (m) is a list of the  
899 variables in the model.